



**HAL**  
open science

## The 2011 Cordón Caulle eruption triggered by slip on the Liquiñe-Ofqui fault system

C. Novoa, Muriel Gerbault, Dominique Rémy, J. Cembrano, L. E. Lara, J. Ruz-Ginouves, A. Tassara, J. C. Baez, R. Hassani, Sylvain Bonvalot, et al.

► **To cite this version:**

C. Novoa, Muriel Gerbault, Dominique Rémy, J. Cembrano, L. E. Lara, et al. The 2011 Cordón Caulle eruption triggered by slip on the Liquiñe-Ofqui fault system. *Earth and Planetary Science Letters*, 2022, 583, 10.1016/j.epsl.2022.117386 . insu-03661484

**HAL Id: insu-03661484**

**<https://insu.hal.science/insu-03661484v1>**

Submitted on 22 Jul 2024

**HAL** is a multi-disciplinary open access archive for the deposit and dissemination of scientific research documents, whether they are published or not. The documents may come from teaching and research institutions in France or abroad, or from public or private research centers.

L'archive ouverte pluridisciplinaire **HAL**, est destinée au dépôt et à la diffusion de documents scientifiques de niveau recherche, publiés ou non, émanant des établissements d'enseignement et de recherche français ou étrangers, des laboratoires publics ou privés.



Distributed under a Creative Commons Attribution - NonCommercial 4.0 International License



30 conditions resulting from the pre-eruptive magma injection. Our results show that such a  
31 magma injection was too small to trigger the eruption. Therefore we explore other eruption  
32 triggers. Analytical elastic inversion models show that the ground displacements observed  
33 during the explosive phase may have been produced by slip motion along a NNW-striking  
34 dextral-strike slip, double-branch fault of the north-trending Liquiñe-Ofqui Fault System  
35 (LOFS), or along a single southern branch fault of the LOFS and collapse of the caldera.  
36 When investigating the elasto-plastic deformation pattern resulting from dextral slip along this  
37 branch-fault system, we obtain a sub-vertical dilatational plastic zone that connects the  
38 reservoir wall to the surface in a location that coincides with that of the 2011 eruption. Hence,  
39 we propose that this LOFS branch-fault eventually destabilized (perhaps weakened by the  
40 2007-2009 episode of magma injection), and then slipped in a way that opened channels for  
41 fluid migration from the magma reservoir up to the surface.

## 43 **1. Introduction**

44 Silicic volcanoes produce the most explosive and hazardous eruptions in the world,  
45 covering large areas with ash and inducing potentially global climatic effects. Therefore,  
46 understanding the mechanisms that control explosive activity is one of the most important  
47 topics in volcanic hazards forecasting. Many active silicic volcanoes are located in the  
48 Southern Volcanic Zone of Chile (SVZ), among which the Puyehue Cordón Caulle Volcanic  
49 Complex (PCCVC) stands as one of the largest and most active.

50 The PCCVC is composed of three main structures trending NW to SE: the ~10 km  
51 wide Cordillera Nevada caldera to the north-west, the ca. 13 km long central Cordón Caulle  
52 fissure system, and the Puyehue stratovolcano to the south-east (**Fig. 1**). Volcanic activity  
53 started ca. 0.5 Ma with a wide range of compositions, evolving to mostly rhyodacitic and  
54 rhyolitic magmas in the Late Pleistocene-Holocene for, both the Cordón Caulle fissure system  
55 and the Puyehue volcano (Lara et al., 2006; Singer et al., 2008). The last three eruptions  
56 (1921, 1960 and 2011) display similar magma compositions, indicating that they were fed by  
57 the same reservoir at depth (Jay et al., 2014). However, they occurred at different places along  
58 the volcanic complex. The 1921 vent was located close to the Cordillera Nevada Caldera  
59 while the two others occurred along the southern and northern flanks of the fissure system  
60 (**Fig. 1**).

61 The 2011 eruption at PCCVC was one of the largest sub-aerial eruptions of the 21st  
62 century. Despite intensive monitoring by geodetic and seismological data, its primary trigger  
63 remains an open issue (Jay et al., 2014; Wendt et al., 2017; Delgado 2020). The eruption was  
64 preceded by an inflation of 22 cm/yr spanning the 2007-2009 period, followed by two years  
65 of barely any ground deformation. Jay et al. (2014) associated this inflation stage with the  
66 injection of 0.05 km<sup>3</sup> of mafic magma in a reservoir located at 4-9 km depth. Considering that

67 this volume of intruded magma was too small to fail the bedrock and, that no direct sign of  
68 ascending magma was observed prior to the eruption, these authors concluded that this pre-  
69 eruptive inflation could not have triggered the 2011 eruption.

70 The 2011 eruption started on June 04 with an explosive phase of pyroclastic ejecta and  
71 gas-venting from a ~10 km high column that lasted 7-9 days (Bonadonna et al., 2015),  
72 followed by lava effusion on June 12-13 until March 2012 (Bertin et al., 2015). During the  
73 explosive phase, a substantial interferometric signal was detected from an ENVISAT  
74 ascending interferogram encompassing the first three days of the eruption, which was  
75 interpreted as mainly due to subsidence (Jay et al., 2014; Wendt et al., 2017). These authors  
76 proposed that this subsidence (reaching about 80 cm) was induced by the volume decrease of  
77 about 0.11 km<sup>3</sup> of two magma bodies located beneath PCCVC at 4 and 6 km depth,  
78 respectively. Nevertheless, the inconsistency between this geodetic volume change at depth  
79 and the volume of erupted tephra (0.27 km<sup>3</sup> DRE) during the first three days of the eruption  
80 led Wendt et al. (2017) to propose an alternative hypothesis. They modeled part of the ground  
81 surface displacement as a closing dyke-like structure with an oblique left-lateral normal  
82 strike-slip motion along the graben. While this proposition provides interesting insights on a  
83 non-magmatic trigger of the eruption, the concept of a closing dyke structure remains  
84 problematic because although it allows the transport of magma to the vent, it fails to explain  
85 where the magma was extracted from.

86 The present paper performs a detailed investigation of the pre-existing tectonic  
87 structures at play during the pre-eruptive and the explosive phase of the 2011 eruption,  
88 associated with the observed InSAR LOS displacement. Combining analytical and finite-  
89 element modeling, we assess the mechanical state of the crust induced by the 2007-2009  
90 magma injection, and then we test two hypotheses of eruption trigger by analyzing elastic and  
91 elasto-plastic strain-stress patterns in the host rock surrounding the magma reservoir.

## 93 **2. The tectono-volcanic setting of PCCVC**

94 In the Southern Andean Volcanic Zone, the N78°E oblique convergence between the  
95 Nazca and South-America plates promotes a regional transpressional regime with the  
96 maximum shortening axis trending N64°E (Cembrano and Lara, 2009; Perez-Flores et al.  
97 2016). Within the SVZ, the 1200 km long margin-parallel Liquiñe-Ofqui Fault System  
98 (LOFS) extends north-south between 36 and 46 °S as a dextral strike-slip fault,  
99 accommodating at present 1 to 7 mm/yr of the ca. 70 mm/yr of plate convergence (e.g.  
100 Stanton-Yonge et al., 2016). Large stratovolcanoes are elongated in the NE-SW direction, but  
101 some also lie along NW-trending directions (Lara et al., 2006; Cembrano and Lara, 2009;  
102 Sielfeld et al., 2019). Small monogenetic eruptive centers in turn are located along the master  
103 fault of the LOFS. It has long been suggested that the NE-trending volcanic alignments  
104 correspond to transtensional domains associated with the dextral transpressional setting of the  
105 arc. In contrast, the NW-oriented volcanic complexes appear controlled by NW transverse  
106 pre-Andean fault systems (Lopez-Escobar et al., 1995; Cembrano and Lara, 2009). Several  
107 studies have argued that during interseismic periods, deformation is partitioned in the arc and  
108 forearc domains, with the activation of N-S trending dextral strike-slip faulting, coeval with  
109 extension along NE-striking structures and sinistral-reverse displacement along NW-striking  
110 inherited structures (Perez-Flores et al. 2016; Sielfeld et al., 2019; Lupi et al., 2020).

111 The Puyehue Cordón Caulle Volcanic Complex (PCCVC, **Fig. 1**) is one of those  
112 volcanic centers lying on top of a basement NW-trending structure, and like others it is  
113 characterized by a wide variety of magma compositions including felsic volcanism, as  
114 opposed to dominantly mafic volcanism along NE-trending domains. López-Escobar et al.,  
115 (1995) proposed that the felsic compositions result from the NW-trending domains being  
116 compressional in nature since they strike nearly orthogonal to the interseismic shortening

117 direction, hereby favoring long-term intra-crustal residence of magma. The Cordón Caulle  
118 geothermal area is located inside a depression that forms a 13km x 6 km, NW-SE elongated  
119 volcano-tectonic corridor hosting numerous monogenetic centers and hot-springs, most of  
120 which stand along its edges (Sepulveda et al., 2005, **Fig. 1**). NE-trending gravimetric profiles  
121 across this depression yield a residual negative anomaly reaching about 20 mGal at its center,  
122 attributed by Sepulveda et al. (2005) to the presence of an infill formed by dacite–rhyolite  
123 lavas and tephra in the first ~ 600 m depth, and which is bordered by inward dipping normal-  
124 like fault zones. Kilometers away where lava cover disappears, exposures of granitic rocks  
125 from the crystalline basement are mostly observed (Lavenu & Cembrano, 1999). Here, as a  
126 first hypothesis for the 2011 eruption trigger, we shall consider the influence of this NW-  
127 oriented caldera-graben structure by considering a mechanically weaker domain.

128         As a second hypothesis for the eruption trigger, we shall consider the influence of a  
129 dextral-slip motion of the LOFS or of one of its numerous branching faults, in consistency  
130 with mapped meso-scale brittle faults and seismological data. On the day of the 2011  
131 eruption, the USGS Catalog reported 22 earthquakes of Mw between 3.6 to 5 and depths  
132 between 3 and 20 km. The focal mechanism of the largest Mw 5.0 event was reported by the  
133 GCMT project, with a dextral-strike slip motion nodal plane consistent with the LOFS  
134 kinematics (**Appendix A1**), and located about 5 kilometers away from the volcanic complex.  
135 We note that a similar focal mechanism was recorded in 1999 for a Mw 5.4 event at 15 km  
136 depth (Cembrano & Lara, 2009) as well as another one in 2010 for a Mw 5.1 event about 90  
137 km further north (CMT Catalog, **Fig. A1**). Our own moment tensor inversion of this event  
138 confirms a dextral strike-slip motion, and re-estimates its location on the fault trace at 7 km  
139 depth (**Appendix A1**). Additionally, satellite images show that the earliest activity of the 2011  
140 explosive eruption was sourced from two cones aligned N18°W (Schipper et al., 2013). This

141 N18°W strike happens to be very close to the N20°W strike of the second nodal plane of the  
142 Mw 5.0 seismic event.

143

### 144 **3. InSAR DATA and processing**

145 The SAR images covering the different periods of activity at PCCVC were acquired by  
146 three satellite missions: L-band Stripmap mode images from ALOS-1 operated by the Japan  
147 Aerospace Exploration Agency (JAXA), C-band ENVISAT ASAR Image Mode data and C-  
148 band Interferometric Wide Swath mode images Sentinel-1A/B, both from the European Space  
149 Agency. All treatment details of the InSAR images are explained in **Appendix A2**.

150

### 151 **4. Determining the geometry of the magmatic reservoir**

152 In a first step we search for the geometry and location of a reliable active source able  
153 to explain the surface displacements observed during the complete eruptive cycle. **Figures 2,**  
154 **3A and B** show the characteristic patterns of ground displacements observed by InSAR data at  
155 PCCVC during the co-eruptive, pre-eruptive and post-eruptive periods. The interferogram of  
156 the co-eruptive explosive phase covers the first 3 days of the eruption. The ground  
157 displacement pattern during this period is characterized by two lobes of slant range increase  
158 (ground moving away from satellite), one of ~ 80 cm located within the Cordillera Nevada  
159 Caldera in the northwestern part of the graben, and the other one of ~30 cm located in the  
160 southeastern part of the graben closer to the eruptive vent (**Fig. 2A**). A lobe of slant range  
161 decrease of ~12 cm is also observed to the north-east of the volcanic complex. In contrast,  
162 during the co-eruptive effusive phase of the eruption from July 2011 to February 2012, the  
163 pattern of ground displacements shows a unique lobe of slant range increase that is



164 consistently oriented NW-SE, centered on the central part of the graben and close to the  
165 eruptive vent (**Fig. 2B**, the interferogram covers December 2011 to February 2012).

166 A similar NW-SE oriented pattern of slant range decrease is clearly identified by visual  
167 inspection of the pre-eruptive ALOS-1 and the post-eruptive Sentinel-1 interferograms (**Fig.**  
168 **3A-B**). Both these interferograms have approximately the same LOS unit look vectors [-  
169 0.6049, -0.1966, 0.7716] and [-0.6113, -0.2093, 0.7660]. This similar pattern suggests that a  
170 similar physical process drove them, leading us to search for a single source geometry able to  
171 explain both pre- and the post-eruptive observed ground displacements.

172 We use two stacks of three ascending and four descending Sentinel-1 interferograms,  
173 and two ALOS1 interferograms to search for the best geometry able to explain ground  
174 displacement at PCCVC (the earliest and the latest images used in the stack are indicated in  
175 Table A2). We assume an uncorrelated uncertainty of 1 and 1.5 cm for Sentinel-1 and ALOS1  
176 data, respectively leading to uncertainties of 6 and 5 mm for the ascending and descending  
177 stacks, respectively.

178 We consider three different sources, including a spherical source (Mogi, 1958), a  
179 prolate spheroid (Yang et al, 1988) and an Okada-type dislocation (Okada, 1985) embedded in  
180 a homogeneous isotropic elastic half-space. Poisson's ratio  $\nu = 0.25$  was assumed as well as  
181 a flat topography, considering that topographic slopes affected by the signal are less than the  
182  $10^\circ$  limit for which their effects become significant (Cayol and Cornet, 1998). The model  
183 fitness is quantified using the weighted root-mean square of the residual phase (rms). We use  
184 a quadtree algorithm to subsample the data points, and a Levenberg-Marquardt algorithm to  
185 minimize the residuals. In agreement with previous studies (Wendt et al., 2017; Delgado  
186 2020) the best model is a prolate spheroidal reservoir yielding an rms of 4.1, 4.7 and 23.8 mm  
187 for the descending and ascending Sentinel-1 stacks, and for ALOS1 data, respectively (Table  
188 1). The source was also inverted using the ascending and descending stacks of Sentinel-1 data

189 conjointly, and yields only a slight increase of the resulting rms. Therefore a prolate  
190 spheroidal source appears a reasonable model to explain pre and post-eruptive surface  
191 displacements, acknowledging that the real medium is certainly more complex than in our  
192 models.

193         Next, we investigate parameters uncertainties for this best-fit model using a Monte-  
194 Carlo simulation. We first estimate the correlated noise from small temporal Sentinel-1 and  
195 ALOS-1 interferograms, and we approximate the InSAR noise using an exponential-type  
196 random noise of variance  $0.8 \cdot 10^{-4} \text{ m}^2$  and of correlation length 5 km. Next, we invert 200  
197 independent trials with added correlated noise to the data, in order to estimate the confidence  
198 interval shown in **Table 1**. ALOS-1 data inversions favor a source located a little further to  
199 the west and striking a little further to the south compared to Sentinel-1 data inversions.  
200 Despite these differences, other parameters range close to each other. We conclude that the  
201 observed inflation during the pre- and post-eruptive periods were driven by a similar  
202 displacement source, best modeled by a prolate-spheroidal reservoir located at 4.5 km depth,  
203 elongated in the  $130^\circ$  direction (N $40^\circ$ W) and with major and minor axes of about 8 km and  
204  $\sim 0.9$  km (**Fig. 3** and **Table 1**). With this geometry, the recorded InSAR pre-eruptive inflation  
205 is explained by a pressure increase ( $\Delta P$ ) of 32 MPa, given a bedrock shear modulus ( $G$ ) of 20  
206 GPa.

207

## 208 **5. Mechanical state associated with the pre-eruptive inflation stage**

209 In order to investigate the pre-eruptive conditions for rock mass failure around the inflating  
210 magma reservoir, we use the finite-element code *Adeli* (details below) to explore stress and  
211 deformation patterns resulting from an overpressure applied at the walls of the prolate-  
212 spheroidal source determined in section 4. Below, we first describe the predicted patterns of  
213 stress and deformation assuming elastic behavior in a homogeneous domain, then in a

214 heterogeneous domain containing a relatively weak caldera-graben structure. Second, elasto-  
 215 plastic rheology is considered to better track strain localization in the overlying crust where  
 216 stresses exceed a failure threshold, for both shear and tensile failure modes. Accounting for  
 217 this rheology allows to infer potentially fractures around the reservoir and their propagation  
 218 throughout the bedrock upon loading, they may constitute pathways for magmatic fluids  
 219 towards the surface.

## 220 **5.1 Numerical method, assumptions and setup**

221 The three-dimensional finite-element code *Adeli* uses the dynamic relaxation method  
 222 (Cundall, 1989) to resolve the quasi-static equation of motion and determine stress and strain  
 223 fields in elastic and elasto-plastic media. This time-explicit method uses an adaptative time-  
 224 step together with damping of out-of-balance forces. It has been used for more than 30 years  
 225 in the engineering (*FLAC* code from *Itasca Consulting Group*) and Earth sciences  
 226 communities, hence implementation details can be found in numerous places (Hassani et al.,  
 227 1997; Cerpa et al., 2015; Gerbault et al., 2018; Novoa et al., 2019; Ruz Ginouves et al., 2021).  
 228 The finite-element mesh is first built using the *GMSH* mesher (illustrations and reference in  
 229 **Appendix A3**). Upon progressive loading, the initially elastic medium starts to yield  
 230 plastically when the yield stress envelope for either Drucker-Prager shear failure ( $F_{DP}$ ) or  
 231 tensile failure ( $F_T$ ) is reached :

$$232 \quad F_{DP}(\sigma) = J_2(\sigma) + \frac{6\sin(\phi)}{3-\sin(\phi)} I_1(\sigma) - \frac{6C\cos(\phi)}{3-\sin(\phi)} = 0, \quad (1)$$

$$233 \quad F_T(\sigma) = I_1(\sigma) - T = 0,$$

234 where  $\phi$  is the friction angle,  $C$  is cohesion,  $T$  tensile strength.  $I_1(\sigma) = \frac{1}{3}tr(\sigma)$  and  $J_2(\sigma) =$   
 235  $\frac{3/2 (s:s)^{1/2}}{\sqrt{2}}$  are first and second invariants of the stress tensor  $\sigma$  ( $s = \sigma - I_1(\sigma).I$  is the  
 236 deviatoric stress tensor). Below we also display the strain invariants  $I_1(\epsilon)$ ,  $J_2(\epsilon)$ , which

237 derive similarly from the strain tensor  $\varepsilon$ . Sign convention is that positive  $I_1(\sigma)$  or  $I_1(\varepsilon)$   
238 describes expansion. Plastic deformation is then determined with an associative flow rule for  
239 tensile failure and a non-associative flow rule for shear failure (here dilatancy is set to zero,  
240 cf. Ruz Ginouves et al., 2021) .

241 All simulations presented below were made assuming zero-friction angle and zero  
242 gravity, in order to reproduce the minimal conditions for plastic failure. This simulates  
243 effective properties of weakened crustal domains due to a variety of processes such as  
244 lithostatic pore-fluid pressure and recurrent micro-fracturing (Sibson, 2003; Suppe, 2014), a  
245 reasonable assumption considering that the PCCVC is one of the most active geothermal  
246 systems of the SVZ. Nevertheless, the reader can find in **Appendix A4** complementary  
247 simulations assuming gravity and a friction angle of  $30^\circ$ , which represents dry and resistant  
248 crust failing at maximal pressure-load conditions.

249 Rewriting Eqs. 1 for zero-friction angle and zero gravity leads to shear failure  
250 initiating when  $J_2(\sigma)=2C$  and tensile failure initiating when  $I_1(\sigma)=T$ . Cohesion and tensile  
251 strengths are chosen proportional to the shear modulus (eg. Schultz et al. 1996), with a  
252 proportionality factor of  $10^{-4}$  equal to that assumed by Zhan et al. (2019) for the Laguna del  
253 Maule Volcanic Complex, also located in the SVZ. For instance, a Young's modulus  $E=50$   
254 GPa (corresponding to a shear modulus  $G=20$  GPa), provides  $C=25$  MPa and  $T=5$  MPa. With  
255 exact values being impossible to assess in the area, we assume a range of values  $E=12.5-50$   
256 GPa,  $C=5-25$  MPa and  $T=1-5$  MPa, compatible with common estimates (Heap et al., 2020).

257

## 258 **5.2 Stress and Strain patterns assuming an Elastic bedrock**

259 First we simulate an overpressurized cavity embedded in a homogeneous elastic medium  
260 (mesh shown in **Appendix A3.1**). The observed  $\sim 40$  cm of LOS surface displacements during

261 the pre-eruptive period can be explained by an overpressurized source ( $\Delta P$ ) of 8 MPa or 32  
262 MPa, given a shear modulus of either 5 GPa or 20 GPa, respectively. Both options produce  
263 the same pattern of dilatation, with maximums at the tips of the spheroid's major axis and  
264 constriction at its roof (**Figs. 4A-B**). These areas of maximum dilatation can be associated  
265 with the opening of micro-fractures promoting seismicity (Simpson et al., 2001; Lamur et al.,  
266 2017), and may explain the seismicity reported in the Cordillera Nevada during the pre-  
267 eruptive period (Wendt et al., 2017). In turn, the constrictional zone at the reservoir's roof  
268 tends to close the pore-space and impede fluid flow between the reservoir and the surface (as  
269 suggested by Gerbault et al., 2018; Zhan et al., 2019).

270 Second, we simulate the caldera-graben system at PCCVC (mesh shown in **Appendix A3.2**),  
271 by inserting a weaker domain around the spheroidal reservoir, of shear modulus  $G=5$  GPa and  
272 embedded in a stiff bedrock of  $G=20$  GPa. An applied overpressure of 8 MPa (fitting surface  
273 displacements), produces dilatational areas mostly identical to the homogeneous case.  
274 However, constriction is intensified inside the compliant caldera-graben domain (**Fig. 4C**,  
275 **Fig. 4D**).

276

### 277 **5.3 Elasto-Plastic Deformation**

278 Then, we explore how bedrock failure might have been at play during the pre-eruptive  
279 inflation period in both these homogeneous and heterogeneous configurations. *Adeli* models  
280 with the failure parameters given above (section 5.1) show that the application of a reservoir  
281 overpressure  $\Delta P=32$  MPa provides first and second stress invariants maxima  $I_1(\sigma)_{\max} = 13$   
282 MPa at the tips of the major axis, and  $J_2(\sigma)_{\max} = 55$  MPa around the minor axes (**Fig. 5A-B-**  
283 **C-D**). Hence, tensile failure expands outwards from the major-axis tips if bedrock tensile  
284 strength  $T < 13$  MPa, while shear failure concentrates along the central minor axis if cohesion  
285  $C < 27.5$  MPa (**Fig. 5E-F-G**). Note that these plastic domains are restricted around the

286 reservoir walls, far from the top surface, which illustrates why the pre-eruptive inflation was  
287 too small to promote an eruption. When we include a weak caldera-graben domain (e.g. the  
288 heterogeneous configuration), similar restricted deformation patterns are produced, leading to  
289 the same conclusion (**Fig. 5H-I**). Numerical simulations show that the reservoir overpressure  
290 would need to be doubled in both configurations for plastic domains to expand and connect  
291 the reservoir and the surface (this stage may be assimilated to the onset of an eruption, e.g.  
292 Gerbault et al., 2018). Furthermore, this connection to the surface occurs near the Cordillera  
293 Nevada, much further to the NW than the actual location of the 2011 eruptive vent (c.f.  
294 Appendix **A4**). Thus in either configurations our numerical simulations show that the pre-  
295 eruptive inflation could not have promoted the eruption. The resulting potential damage zones  
296 remain constrained close to the reservoir walls and never approach the location of the 2011  
297 eruption. These results combined with the fact that no inflation was observed at the PCCVC's  
298 surface during the two years prior to the eruption, lead us to eliminate a magmatic inflow  
299 trigger.

300

## 301 **6. Kinematic models of a tectonic trigger to the co-eruptive explosive phase**

302 We explore now the possibility that slip along one of the tectonic structures identified  
303 in the area may have triggered the 2011 eruption. As a preliminary step, we need to subtract  
304 how much of the observed slant range increase associated with the explosive phase of the  
305 eruption could be attributed to the reservoir's emptying at depth. Therefore we estimate the  
306 volume change of the prolate reservoir during the explosive phase using (Mastin et al. 2008):

$$307 \quad \frac{V_e}{DV} = -\left(1 + \frac{K_m}{K_r}\right) \quad (2)$$

308 Taking into account the erupted volume ( $V_e$ ), estimated by Pistolesi et al. (2015), the  
309 compressibility of the bedrock ( $K_r$ ) and the magma ( $K_m$ ) inferred by Wendt et al., (2017) and

310 Jay et al. (2014), respectively, the volume change associated with this deep source must have  
311 been of the order of 0.03 km<sup>3</sup>. This volume change can only account for about 20% of the  
312 subsidence observed during the first 3 days of the eruption, supporting the argument that the  
313 other 80% of cumulated InSAR displacements must have a non-magmatic origin.

314 Next, we search for the best location and geometry of fault planes characterizing  
315 nearby tectonic structures. Two disconnected faults structures are identified and are each  
316 subdivided into multiple dislocation patches. To best fit the observed InSAR displacement  
317 resulting from slip along these patches, we compute ground surface displacements using the  
318 inversion algorithm provided by the Principal Component Analysis-based Inversion Method  
319 (PCAIM) software, which uses Okada's equations as Green's functions throughout an elastic  
320 medium (Kositsky and Avouac, 2010; Perfettini et al., 2010, technical details in **Appendix**  
321 **A5**). In the following, the corresponding geodetic moments are also estimated, assuming  $G=$   
322 20 GPa in the bedrock.

### 323 **6.1 Testing slip motion along the Caldera-Graben structure**

324 As a first hypothesis, we investigate if a combination of downdip slip along the  
325 Cordillera Nevada and reverse-sinistral slip along the graben walls (consistent with the  
326 structural data mentioned in **Section 2**) can explain the remaining subsidence observed during  
327 the explosive phase. We use the fault system geometry defined in section 5.2 and discretize it  
328 into 902 elementary patches  $1.1 \times 1.4 \text{ km}^2$  in size. In the PCAIM inversion, we constrain the  
329 rake angle and direction to normal in the Cordillera Nevada caldera, and to reverse-sinistral  
330 slip along the graben walls. In the end we could not obtain a satisfactory model fitting the  
331 InSAR data with this geometry, because we always need to extend the limit of the northern  
332 wall of the graben much further to the south-east than actually mapped (segment C-D in **Fig.**  
333 **6.A**). This leads us to discard this hypothesis.

## 334 6.2 Testing slip motion along a branch fault of the LOFS

335 As a second hypothesis, we assess if the LOS displacement during the explosive phase  
336 of the eruption could be related to the activation of a branch of the LOFS. Therefore, we take  
337 the most north-south oriented plane deduced from the Mw 5.0 focal mechanism, whose  
338 location coincides with a fault trace inferred by the OVDAS (**Appendix A1**). This nodal plane  
339 resembles the main trace of the LOFS, which is generally described as a subvertical fault zone  
340 (e.g., Sielfeld et al., 2019; Díaz et al., 2020). We use this assumption considering that at the  
341 scale of the PCCVC, the LOFS cannot be recognized from geomorphological features nor  
342 from the geophysical record. It is however supported by the N-S alignment of minor eruptive  
343 centers south of Puyehue volcano (Lara et al., 2006), an orientation that is also observed in  
344 other segments along the SVZ and that is thought to serve as pathways for primary basalts  
345 along the arc (Cembrano and Lara, 2009; McGee et al., 2017). There is also evidence of a  
346 near-vertical NS-trending fault from the geological record (Cembrano et al., 1996; Lavenu  
347 and Cembrano, 1999), where deformed rocks are now exhumed and eroded by glaciers  
348 shaping a large-scale fault system. The resulting fault zone is discretized into 638 elementary  
349 patches  $1.2 \times 1.4 \text{ km}^2$  in size, for inversion with PCAIM based on InSAR data. The best  
350 fitting model displays two slipping patches leading to a variance reduction of 86 % and a rms  
351 = 0.05 m (**Fig. 6B**). This model fits InSAR data reasonably well, but systematic residuals  
352 remain visible near the fault trace. The biggest slipping patch is located to the north east of the  
353 graben, with a length of 15 km and a width of 7 km, while the smaller one is located to the  
354 south of the graben with a length of 7 km and a width of 6 km (**Fig. 6B**). These northern and  
355 southern slip patches each imply a geodetic moment of about  $2.4 \times 10^{18} \text{ N}\cdot\text{m}$  and  $6.1 \times 10^{17}$   
356  $\text{N}\cdot\text{m}$ , respectively (discussed in section 7).

## 357 6.3 Slip motion along the southern branch-fault of the LOFS and Caldera collapse



358           The two hypotheses above lead us to propose a third scenario, which assesses the  
359 possibility that the LOS displacements were caused by a collapse of the Cordillera Nevada  
360 and concomitant slip motion along the southern branch-fault of the LOFS. Inversions of the  
361 LOS displacement in the vicinity of the caldera (section **6.1**) combined with the Okada-model  
362 constrained by the CMT focal mechanism along the southern-branch fault (section **6.2**),  
363 provides a best fitting model explaining 92 % of the variance with a rms of 0.042 m. The  
364 patch located on the wall of the Cordillera Nevada Caldera provides a mean amount of slip of  
365 about 1.25 m onto a ~10 km-deep and ~15 km-long fault surface (**Fig. 6C**). The geodetic  
366 moments associated with these two slipping patches yield  $3.77 \times 10^{18}$  N·m and  $2.23 \times 10^{17}$  N·m,  
367 respectively.

368

## 369 **7. Discussion**

### 370 **7.1 Geometry of the magmatic reservoir at PCCVC**

371           The inversion of both pre- and post-eruptive InSAR ground displacements suggests  
372 that deformation was driven by inflation of a source of similar shape. Nevertheless, this  
373 similarity in shape remains difficult to link with the pattern of InSAR ground displacement  
374 during the effusive phase, which has been interpreted as mainly resulting from the emptying  
375 reservoir (Delgado 2020; **Fig. 2B**). This explains why the temporal and spatial patterns of  
376 ground displacement had previously been interpreted with magma injection sources at  
377 different and independent locations, for the pre- and post-eruptive periods (Jay et al., 2014;  
378 Wendt et al., 2017; Delgado 2020). While these interpretations offer the possibility to explain  
379 the ground displacements during the different phases of the volcanic cycle, they fail in  
380 providing a consistent framework for the evolution of the shallow magma plumbing system.  
381 The striking difference in pattern of ground displacement between the effusive phase and the

382 pre- and post-eruptive phases suggests that it could have resulted from damaging of the  
383 shallow magma plumbing system and/or of the overlying hydrothermal system.

## 384 **7.2 Kinematic models for the explosive phase of the eruption**

385         Whereas 20% of the InSAR-observed subsidence is explained by 0.03 km<sup>3</sup> of  
386 decreasing volume of the magma reservoir, the remaining 80% can be accounted for by a  
387 kinematic model of motion along a branch-fault of the LOFS, accompanied or not by the  
388 collapse of the caldera (**Figs. 6B-C**). While the former model fits data slightly better (rms of  
389 0.042 vs. 0.05 m), differences are small. In both solutions, systematic localized residuals are  
390 visible probably because of the simplified assumptions of the structures geometry and  
391 rheology. These two models yield a geodetic moment release during the explosive phase of  
392 the eruption of  $3.01 \times 10^{18}$  and  $3.99 \times 10^{18}$  N·m, respectively. In comparison, the 22 seismic  
393 events reported by the USGS catalog on the first day of the eruption reach a total seismic  
394 moment of about  $2.35 \times 10^{17}$  N·m, corresponding to a seismic magnitude  $M_w = 5.5$ . This yields  
395 a geodetic/seismic ratio ranging from 13 to 17, depending on the model. Such high moment  
396 ratios have been observed in other volcanic areas worldwide and authors have suggested that  
397 a large proportion of the stress energy is likely released aseismically rather than by brittle  
398 failure (Langbein et al., 1993; Pedersen et al., 2007). Note that moment ratios must be  
399 invoked with caution since they are determined with an order of magnitude of uncertainty  
400 (Pedersen et al., 2007).

## 401 **7.3 Role of a branch of the LOFS based on surface observations**

402         Our kinematical models (section 6) suggest that right-lateral normal slip motion along  
403 a branch fault of the LOFS played an essential role during the explosive phase of the 2011  
404 eruption. This scenario differs from that of Wendt et al. (2017) of a closing dyke with a left-  
405 lateral normal strike-slip motion along the northern flank of the graben. As mentioned above,

406 the activation of a LOFS branch is strongly supported by independent seismic data, structural  
407 field observations and available petrological data (section 2). In addition, structural and  
408 satellite data show *en-échelon* fracture segments and aligned ground cracks in directions  
409 parallel to an overlapping cone structure striking N18°W (Schipper et al., 2013). The  
410 coincident location and strike of these structures with the buried fault obtained in our  
411 inversion model, strengthens this interpretation. Finally, failure along a fault plane is also  
412 invoked by Castro et al. (2013) to explain the transport of magma from depth to the vent at  
413 very slow rates (~1 cm/yr).

414 Slip motion along the LOFS also provides insight into the transition of the eruption  
415 style from explosive to effusive: the coincident orientation of the vents, the inverted fault  
416 plane and the location of the seismic swarm during the explosive phase all indicate that this  
417 fault zone itself may have been the channel along which the magma rose to the surface. Based  
418 on the coincident depth of the reservoir inferred from petrological data (2-5 km) and that of  
419 the shallow seismicity reported two days before the eruption (2-6 km), Castro et al. (2013)  
420 suggested that rock fracturing occurred in association with the creation of a dyke-like conduit  
421 that fed the vent. Therefore, we propose that the transition from the explosive to the effusive  
422 phases was associated with the transition from a shear-slipping fracture that allowed the  
423 magma to degas, to its opening as a dyke through which magma withdrawal occurred and  
424 reached the surface. A similar mechanism is also suggested for caldera collapses within strike-  
425 slip tectonic regimes (e.g., Holohan et al., 2008).

#### 426 **7.4 Possible mechanisms triggering the 2011 eruption**

427 Our models of a magmatic overpressurization induce dilatation at the shallowest tip of  
428 the reservoir located beneath the Cordillera Nevada Caldera. Such dilatational domains can  
429 mobilize fluids and promote seismicity (references in section 5.2). Similarly to Lundgren et  
430 al. (2020) and Zhan et al. (2019), we suggest that the seismicity reported between 2007-2011

431 beneath the Cordillera Nevada Caldera resulted from such a dilatation induced by magmatic  
432 injection during the pre-eruptive period (**Fig. 4B**). Our models also show that constriction  
433 around the inflating reservoir does not facilitate magmatic fluid flow towards the surface (**Fig.**  
434 **4C-D**), and thus rather inhibits an eruption. Whereas the lack of substantial pre-eruptive  
435 inflation observed by InSAR in the two years prior to the eruption leads us to discard magma  
436 supply from depth as the 2011 eruption trigger, we cannot exclude the possibility that a short-  
437 lived pre-eruptive inflation was compensated by co-eruptive deflation in a single orbital cycle.  
438 The other scenario of a caldera collapse alone, which would have triggered reservoir  
439 withdrawal and the eruption of magma, requires a tensile state of stress across the caldera-  
440 graben structure, and normal slip along the caldera and graben walls. This is inconsistent with  
441 the regional interseismic state of compression expected at PCCVC. While Gudmundsson  
442 (1998) argued that extension could be induced by flexural doming of a deeper pressure source  
443 under the shallow chamber, here there is no evidence of large-scale precursory inflation at  
444 PCCVC. However, once again we cannot exclude that the amplitude of ground displacement  
445 induced by a deep source was below the accuracy of radar sensors, or was compensated by the  
446 co-eruptive deflation.

447         Several studies have suggested that the seismic cycle of subduction megathrusts plays  
448 a key role in modifying the stress field in the overriding plate and promoting transient tensile  
449 stresses (Walter and Amelung, 2007). While Lara et al. (2006) proposed that the recurrent  
450 shearing of pre-existent faults at PCCVC causes transient stress field rotations, promoting the  
451 ascent of magma within coeval tensile conditions, there is no evidence that the 2011 Cordón  
452 Caulle eruption was directly triggered by the 2010 Maule mega-earthquake: first, the latter  
453 occurred far away (~500 km to the north), and second, according to Bonali et al. (2015) it  
454 rather exerted a clamping of the PCCVC area, tending to impede any eruption.

455           Consequently, we need to search for another triggering mechanism to the 2011 Cordon  
456   Caulle eruption.

## 457   **7.5 The slipping LOFS branch hypothesis**

458           The last mechanism that could lead to draining of the magma chamber would be slip  
459   motion along a branch of the LOFS. Hence, we investigate now, how motion along a branch-  
460   fault of the LOFS could have triggered the eruption by setting up additional 3D models that  
461   explore such a fault-reservoir interaction (mesh shown in **Appendix A3.3**). First we check the  
462   response of this configuration to a pre-inflation with  $\Delta P = 32$  MPa: assuming elastic behavior,  
463   **Fig. 7** shows constriction in the fault domains closest to the reservoir, which are squeezed by  
464   the expanding stiffer surrounding bedrock. However, further away along the fault domain,  
465   constriction switches to dilatation (positive volumetric strain); this may increase porosity,  
466   favor the release of interseismic pre-existing stress and drive magmatic fluid pathways (eg.  
467   Ruz Ginouves et al., 2021). Then considering elasto-plasticity, even low fault strength values  
468   such as  $T = 1$  MPa and  $C = 5$  MPa generate only a restricted plastic domain. Inflation does not  
469   trigger surface failure and is too small to be detected by InSAR observations.

470           Second, we apply slip motion along the walls of these fault zones, with magnitudes  
471   consistent with the geodetic moment obtained from the inversions (section **6.2**). This fault  
472   activation promotes dilatation and constriction at the edges of the fault planes (**Fig. 8A**). At  
473   reservoir depths, the induced dilatation exceeds by  $\sim 3$  times the dilatation predicted during the  
474   pre-eruptive period (**Fig. 5A** vs. **Fig. 8A**), and the shear stress is potentially  $\sim 7$  times greater  
475   (**Fig. 5C** vs. **8B**). With cohesion and tensile strength identical to the pre-eruptive  
476   configuration, this elasto-plastic model now predicts shear failure along the entire fault zone,  
477   and tensile failure in the bedrock between the fault zone and the reservoir, **Figure 8C**. In  
478   contrast to the pre-eruptive inflation models, this plastic dilatation domain develops through  
479   the bedrock and connects the reservoir with the surface, in the SE part of the PCCVC where

480 the vent actually occurred (**Fig. 8D-E-F**). This sub-vertical dilatational domain can be  
481 interpreted as a channel that opens the bedrock pore space from which magmatic fluids can  
482 migrate all the way up to the surface (pathways 1-2 in **Fig. 8D-E-F**). Dilatation at the surface  
483 encompasses the location of the swarm of shallow seismicity reported by Wendt et al., (2017)  
484 a few days before the eruption (**Fig. 8F**). We note that pathway (1) may have been impeded  
485 with respect to pathway 2 because first, constriction during the pre-eruptive phase counter-  
486 acts dilatation, and second, constriction close to the surface impedes magma out-flow.

487         The activation of a NNW-striking LOFS branch stands as the best candidate scenario  
488 to explain the 2011 Cordón Caulle eruption. In terms of timing, it is difficult to discern the  
489 exact moment when slip may have started on this fault. Based on the change in location of  
490 seismicity presented by Wendt et al., (2017) we suggest that it may have occurred a few days  
491 before the eruption. Our hypothesis is also consistent with Lara et al. (2006)'s proposition that  
492 shearing of pre-existent faults promotes magma ascent within transient tensile conditions, in a  
493 way similar to other studies (e.g. Diez et al., 2005).

## 494 **7.6 Triggering of historical eruptions**

495         The last three eruptions at PCCVC occurred at different places, along the ring faults of  
496 the Cordillera Nevada Caldera in 1921 and along the opposite edges of the Cordón Caulle  
497 graben in 1960 and in 2011 (**Fig. 1**). Geological mapping shows that this pattern is repeated  
498 for the older units thus evidencing a long-term behavior. Our simulations show that when  
499 considering a sufficient overpressure in the reservoir, the connection of the plastically yielded  
500 domain between the reservoir and the surface occurs in the NW section of the PCCVC, under  
501 the Cordillera Nevada Caldera and the NW portion of the graben. Consequently, we suggest  
502 that the 1921 eruption and those previously fed from vents located along the ring faults likely  
503 had a dominantly magmatic origin.

504           While the 2011 eruption would have responded to a combination of magmatic and  
505 tectonic forcing, none of the mechanisms explored here explain the location of the 1960  
506 eruption at PCCVC, which occurred along the graben's southern wall. This eruption occurred  
507 only 36 hours after the Mw 9.5 Valdivia earthquake (Barrientos et al., 1994), just in front of  
508 the major rupture zone. In relation to the argument cited above that the seismic cycle is able to  
509 modify the regional stress field (Manga & Brodsky, 2006; Walter and Amelung, 2007), Lara et  
510 al. (2004) argued that co-seismic extension inland promoted reshearing of the NW faults  
511 along the graben, and generated a transient transtensional pattern that favored the eruption.  
512 Moreover, the 2015 eruptive activity at Nevados de Chillan was also linked to the 2010 Maule  
513 earthquake (Lupi et al., 2020). Future modeling should investigate the rotation of the regional  
514 stress field due to far-field subduction earthquakes. The constraints provided by our models  
515 here combined with those of Lara et al. (2004) feed the discussion about remote triggering of  
516 volcanic eruptions.

517

## 518 **8. Conclusions**

519           In this study we used geodetic data recorded before, during and after the 2011 Cordon  
520 Caulle eruption, to understand the mechanical conditions associated with its eruptive cycle.  
521 We found that the ground displacements observed before and after the eruptive event can be  
522 linked with a similar inflating source, suggesting that the geometry of the shallow plumbing  
523 system regained its pre-eruptive shape. Nevertheless, the subsidence observed during the  
524 explosive phase of the eruption requires an additional cause, for which we tested two  
525 hypotheses implying fault slip motion.

526           Our results indicate that part of the observed subsidence during the explosive phase  
527 was due to dextral-slip motion along a pre-existing NNW-striking branch-fault of the LOFS.

528 The pre-eruptive magmatic inflation potentially weakened this branch-fault, which would  
529 have been reactivated before the eruption.

530 We relate this dextral-strike slip motion to the earthquake swarm including the Mw 5.0  
531 earthquake that occurred quasi-simultaneously with the onset of the eruption. The greater  
532 geodetic moment deduced from our analysis than the seismic moment released by the swarm  
533 suggests that this slip motion was mainly aseismic. However, the lack of continuous GNSS  
534 recording stations in the vicinity of LOFS prior to the eruption makes it impossible to  
535 determine a precise timing of this slow slip event. We propose that this largely aseismic slip  
536 motion changed the local stress state from compressive to tensile within the volcanic  
537 complex, leading to magma rising to the surface.

538 Although standard elastic models provide good information to constrain the geometry,  
539 location and overpressure conditions on a magma reservoir from the inversion of observed  
540 surface displacements, 3D elasto-plastic models accounting for rheological heterogeneities  
541 help assessing the mechanical state, the potential weakening induced by magmatic injection,  
542 and the tectonic trigger of explosive eruptions. In that line, 3D numerical methods accounting  
543 for non-linear (poro-visco-elasto-plasticity) rheology will soon become essential to move  
544 forward in understanding silicic eruptions.

545

## 546 **Acknowledgements**

547 This work was made possible thanks to a PhD scholarship granted to Camila Novoa  
548 Lizama by CONYCIT-Becas Chile (folio 72170643). Interactions between co-authors were  
549 greatly facilitated by the franco-chilean ECOS-Sud project C18U01. JCB was supported by  
550 FONDECYT1200779 and ANID PIA ACT192169. Francisco Delgado is thanked for  
551 insightful discussions at the onset of this study. The models were ran on the OMP community  
552 cluster Nuwa (<http://www.aero.obs-mip.fr/parc-instru/platmod>). ASAR data were provided



553 by the European Space Agency (ESA) through the project ENVISAT-AO#857 and Category 1  
554 #2899. PALSAR data from the ALOS satellite mission operated by the Japanese Aerospace  
555 Exploration Agency (JAXA) were used under the terms and conditions of the fourth ALOS 2  
556 Research Announcement (project 1142). We thank the European Space Agency for providing  
557 us SENTINEL and ENVISAT data. We thank the editor Jean-Philippe Avouac and the two  
558 anonymous reviewers for their helpful and constructive suggestions that greatly improved this  
559 study.

560

561

## 562 References

- 563 Barrientos, S. E. (1994). Large thrust earthquakes and volcanic eruptions. *Pure and Applied Geophysics*  
 564 *PAGEOPH*. <https://doi.org/10.1007/BF00875972>.
- 565 Bertin, D., Lara, L. E., Basualto, D., Amigo, A., Cardona, C., Franco, L., Gil, F., & Lazo, J. (2015). High  
 566 effusion rates of the Cordón Caulle 2011-2012 eruption (Southern Andes) and their relation with the quasi-  
 567 harmonic tremor. *Geophysical Research Letters*. <https://doi.org/10.1002/2015GL064624>.
- 568 Bonadonna, C., Pistolesi, M., Cioni, R., Degruyter, W., Elissondo, M., & Baumann, V. (2015). Dynamics of  
 569 wind-affected volcanic plumes: The example of the 2011 Cordón Caulle eruption, Chile. *Journal of Geophysical*  
 570 *Research: Solid Earth*. <https://doi.org/10.1002/2014JB011478>.
- 571 Bonali, F. L., Tibaldi, A., & Corazzato, C. (2015). Sensitivity analysis of earthquake-induced static stress  
 572 changes on volcanoes: The 2010Mw 8.8 Chile earthquake. *Geophysical Journal International*.  
 573 <https://doi.org/10.1093/gji/ggv122>.
- 574 Castro, J. M., Cordonnier, B., Schipper, C. I., Tuffen, H., Baumann, T. S., & Feisel, Y. (2016). Rapid laccolith  
 575 intrusion driven by explosive volcanic eruption. *Nature Com.* <https://doi.org/10.1038/ncomms13585>.
- 576 Cembrano, J., Hervé, F., & Lavenu, A. (1996). The Liquiñe Ofqui fault zone: a long-lived intra-arc fault system  
 577 in southern Chile. *Tectonophysics*, 259(1-3), 55-66.
- 578 Cembrano, J., Lara, L. (2009). The link between volcanism and tectonics in the southern volcanic zone of the  
 579 Chilean Andes: A review. *Tectonophysics*. <https://doi.org/10.1016/j.tecto.2009.02.038>.
- 580 Cerpa, N. G., Araya, R., Gerbault, M., Hassani, R. (2015) Relationship between slab dip and topography  
 581 segmentation in an oblique subduction zone : insights from numerical modeling *Geophys. Res. Lett.*,  
 582 [doi.org/10.1002/2015GL064047](https://doi.org/10.1002/2015GL064047).
- 583 Cundall, P.I. 1989. Numerical experiments on localization in frictional materials. *Ingenieur-archiv*, 59(2), 148-  
 584 159.
- 585 *Delgado, F. (2020). Rhyolitic volcano dynamics in the Southern Andes: Contributions from 17 years of InSAR*  
 586 *observations at Cordón Caulle volcano from 2003 to 2020. Journal of South American Earth Sciences.*  
 587 <https://doi.org/10.1016/j.jsames.2020.102841>
- 588 Díaz, D., Zúñiga, F., & Castruccio, A. (2020). The interaction between active crustal faults and volcanism: A  
 589 case study of the Liquiñe-Ofqui Fault Zone and Osorno volcano, southern Andes, using  
 590 magnetotellurics. *Journal of Volcanology and Geothermal Research*, 393, 106806.
- 591 Díez, M., La Femina, P. C., Connor, C. B., Strauch, W., & Tenorio, V. (2005). Evidence for static stress changes  
 592 triggering the 1999 eruption of Cerro Negro Volcano, Nicaragua and regional aftershock sequences. *Geophysical*  
 593 *Research Letters*. <https://doi.org/10.1029/2004GL021788>.
- 594 Fournier, T. J., Pritchard, M. E., & Riddick, S. N. (2010). Duration, magnitude, and frequency of subaerial  
 595 volcano deformation events: New results from Latin America using InSAR and a global synthesis. *Geochemistry,*  
 596 *Geophysics, Geosystems*. <https://doi.org/10.1029/2009GC002558>.
- 597 Gerbault, M., Hassani, R., Novoa Lizama, C., & Souche, A. (2018). Three-Dimensional Failure Patterns around  
 598 an Inflating Magmatic Chamber. *Geochemistry, Geophysics, Geosystems*. [doi.org/10.1002/2017GC007174](https://doi.org/10.1002/2017GC007174).
- 599 Ginouves Ruz, J., Gerbault, M., Cembrano, J., Iturrieta, P., Leiva, F. S., Novoa, C., & Hassani, R. (2021). The  
 600 interplay of a fault zone and a volcanic reservoir from 3D elasto-plastic models: Rheological conditions for  
 601 mutual trigger based on a field case from the Andean Southern Volcanic Zone. *Journal of Volcanology and*  
 602 *Geothermal Research*, 107317.
- 603 Gudmundsson, A. (1998). Formation and development of normal-fault calderas and the initiation of large  
 604 explosive eruptions. *Bulletin of Volcanology*, 60(3), 160-170.
- 605 Hassani R., Jongmans, D., Chéry, J. (1997). Study of plate deformation and stress in subduction processes  
 606 using two-dimensional numerical models. *J. Geophys. Res.* 102(B8), 17951-17965.
- 607 Heap, M. J., Villeneuve, M., Albino, F., Farquharson, J. I., Brothelande, E., Amelung, F., et al. (2020). Towards  
 608 more realistic values of elastic moduli for volcano modelling. *J. Volc. Geoth. Res.*, 390, 106684.
- 609 Holohan, E. P., Van Wyk de Vries, B., & Troll, V. R. (2008). Analogue models of caldera collapse in strike-slip  
 610 tectonic regimes. *Bulletin of Volcanology*. <https://doi.org/10.1007/s00445-007-0166-x>.

- 611 Ingebritsen, S. E., & Gleeson, T. (2015). Crustal permeability: Introduction to the special issue. *Geofluids*.  
612 <https://doi.org/10.1111/gfl.12118>.
- 613 Jay, J., Costa, F., Pritchard, M., Lara, L., Singer, B., & Herrin, J. (2014). Locating magma reservoirs using  
614 InSAR and petrology before and during the 2011-2012 Cordón Caulle silicic eruption. *Earth and Planetary  
615 Science Letters*. <https://doi.org/10.1016/j.epsl.2014.03.046>.
- 616 Kositsky, A. P., & Avouac, J. P. (2010). Inverting geodetic time series with a principal component analysis-based  
617 inversion method. *Journal of Geophysical Research: Solid Earth*. <https://doi.org/10.1029/2009JB006535>.
- 618 Lamur, A., Kendrick, J. E., Eggertsson, G. H., Wall, R. J., Ashworth, J. D., & Lavallée, Y. (2017). The  
619 permeability of fractured rocks in pressurised volcanic and geothermal systems. *Scientific Reports*.  
620 <https://doi.org/10.1038/s41598-017-05460-4>.
- 621 Lara, L. E., Naranjo J.A., and H. Moreno (2004). Rhyodacitic fissure eruption in Southern Andes (Cordón  
622 Caulle; 40.5 S) after the 1960 (Mw: 9.5) Chilean earthquake: a structural interpretation. *Journal of Volcanology  
623 and Geothermal Research* 138, 1-2, 127-138.
- 624 Lara, L. E., Moreno, H., Naranjo, J. A., Matthews, S., & Pérez de Arce, C. (2006). Magmatic evolution of the  
625 Puyehue-Cordón Caulle Volcanic Complex (40° S), Southern Andean Volcanic Zone: From shield to unusual  
626 rhyolitic fissure volcanism. *Journal of Volcanology and Geothermal Research*.  
627 <https://doi.org/10.1016/j.jvolgeores.2006.04.010>.
- 628 Lavenu, A., & Cembrano, J. (1999). Compressional- and transpressional-stress pattern for Pliocene and  
629 Quaternary brittle deformation in fore arc and intra-arc zones (Andes of Central and Southern Chile). *Journal of  
630 Structural Geology*. [https://doi.org/10.1016/S0191-8141\(99\)00111-X](https://doi.org/10.1016/S0191-8141(99)00111-X).
- 631 Langbein, J., Hill, D. P., Parker, T. N., and Wilkinson, S. K. (1993), An episode of reinflation of the Long Valley  
632 Caldera, eastern California: 1989–1991, *J. Geophys. Res.*, 98( B9), 15851– 15870, doi:[10.1029/93JB00558](https://doi.org/10.1029/93JB00558).
- 633 López Escobar, Á., Cembrano, J., & Moreno, H. (1995). Geochemistry and tectonics of the Chilean Southern  
634 Andes basaltic Quaternary volcanism (37–46°S). *Andean Geology*. <https://doi.org/10.5027/andgeoV22n2-a06>.
- 635 Lundgren, P., Girona, T., Bato, M. G., Realmuto, V. J., Samsonov, S., Cardona, C., Franco, L., Gurrola, E., &  
636 Aivazis, M. (2020). The dynamics of large silicic systems from satellite remote sensing observations: the  
637 intriguing case of Domuyo volcano, Argentina. *Scientific Reports*. <https://doi.org/10.1038/s41598-020-67982-8>.
- 638 Lupi, M., Trippanera, D., Gonzalez, D., D'amico, S., Acocella, V., Cabello, C., Stef, M. M., & Tassara, A.  
639 (2020). Transient tectonic regimes imposed by megathrust earthquakes and the growth of NW-trending volcanic  
640 systems in the Southern Andes. *Tectonophysics*. <https://doi.org/10.1016/j.tecto.2019.228204>.
- 641 McGee, L. E., Brahm, R., Rowe, M. C., Handley, H. K., Morgado, E., Lara, L. E., ... & Valdivia, P. (2017). A  
642 geochemical approach to distinguishing competing tectono-magmatic processes preserved in small eruptive  
643 centres. *Contributions to Mineralogy and Petrology*, 172(6), 44.
- 644 Manga, M., & E. Brodsky. Seismic triggering of eruptions in the far field: Volcanoes and geysers (2006). *Annu.  
645 Rev. Earth Planet. Sci.* 34, 263-291.
- 646 Mastin, L. G., Roeloffs, E., Beeler, N. M., and Quick, J. E. (2008). Constraints on the size, overpressure, and  
647 volatile content of the mount st. helens magma system from geodetic and dome-growth measurements during the  
648 2004–2006 eruption. *US Geol. Surv. Prof. Pap.* 1750:461–488.
- 649 McCaffrey, Robert. (1996). Slip partitioning at convergent plate boundaries of SE Asia. *Geological Society  
650 Special Publication*. <https://doi.org/10.1144/GSL.SP.1996.106.01.02>.
- 651 Mogi K. (1958), Relations between the eruptions of various volcanoes and the deformation of the ground surface  
652 around them, *Bull. Earthquake Res. Inst.*, Univ. Tokyo , 36, 99–134.
- 653 Novoa, C., Remy, D., Gerbault, M., Baez, J. C., Tassara, A., Cordova, L., Cardona, C., Granger, M., Bonvalot,  
654 S., & Delgado, F. (2019). Viscoelastic relaxation: A mechanism to explain the decennial large surface  
655 displacements at the Laguna del Maule silicic volcanic complex. *Earth and Planetary Science Letters*.  
656 <https://doi.org/10.1016/j.epsl.2019.06.005>.
- 657 Pedersen, R., Sigmundsson, F., and Einarsson, P. (2007). Controlling factors on earthquake swarms associated  
658 with magmatic intrusions; Constraints from Iceland. *J. Volcanol. Geotherm. Res.* 162, 73–80. doi:  
659 10.1016/j.jvolgeores.2006.12.01

- 660 Okada Y. (1992), Internal deformation due to shear and tensile faults in a half-space, *Bull. Seismol. Soc. Am.* 82,  
661 1018–1040.
- 662 Pérez-Flores, P., Cembrano, J., Sánchez-Alfaro, P., Veloso, E., Arancibia, G., & Roquer, T. (2016). Tectonics,  
663 magmatism and paleo-fluid distribution in a strike-slip setting: Insights from the northern termination of the  
664 Liquiñe-Ofqui fault System, Chile. *Tectonophysics*. <https://doi.org/10.1016/j.tecto.2016.05.016>.
- 665 Pistolesi, M., Cioni, R., Bonadonna, C., Elissondo, M., Baumann, V., Bertagnini, A., ... & Francalanci, L. (2015).  
666 Complex dynamics of small-moderate volcanic events: the example of the 2011 rhyolitic Cordón Caulle  
667 eruption, Chile. *Bulletin of Volcanology*, 77(1), 1-24.
- 668 Schipper, C. I., Castro, J. M., Tuffen, H., James, M. R., & How, P. (2013). Shallow vent architecture during  
669 hybrid explosive-effusive activity at Cordón Caulle (Chile, 2011-12): Evidence from direct observations and  
670 pyroclast textures. *Journal of Volcanology and Geothermal Research*.  
671 <https://doi.org/10.1016/j.jvolgeores.2013.06.005>.
- 672 Schultz, R.A. (1996). Relative scale and the strength and deformability of rock masses. *J. Struct. Geol.* 18(9),  
673 1139-1149.
- 674 Sepúlveda, F., Lahsen, A., Dorsch, K., Palacios, C., & Bender, S. (2005). Geothermal Exploration in the Cordón  
675 Caulle Region , Southern Chile. *World Geothermal Congress 2005*.
- 676 Sibson, R.H. (2003). Brittle-failure controls on maximum sustainable overpressure in different tectonic regimes.  
677 *AAPG Bulletin*, 87(6), 901-908. DOI: 10.1306/0129030018.
- 678 Sielfeld, G., Lange, D., & Cembrano, J. (2019). Intra-Arc Crustal Seismicity: Seismotectonic Implications for  
679 the Southern Andes Volcanic Zone, Chile. *Tectonics*. <https://doi.org/10.1029/2018TC004985>.
- 680 Simpson, G., Guéguen, Y., & Schneider, F. (2001). Permeability enhancement due to microcrack dilatancy in the  
681 damage regime. *J. Geophys. Res.*, 106(B3), 3999-4016.
- 682 Singer, B. S., Jicha, B. R., Harper, M. A., Naranjo, J. A., Lara, L. E., & Moreno-Roa, H. (2008). Eruptive history,  
683 geochronology, and magmatic evolution of the Puyehue-Cordón Caulle volcanic complex, Chile. *Geological*  
684 *Society of America Bulletin*, 120(5-6), 599-618.
- 685 Stanton-Yonge, A., Griffith, W. A., Cembrano, J., St. Julien, R., & Iturrieta, P. (2016). Tectonic role of margin-  
686 parallel and margin-transverse faults during oblique subduction in the Southern Volcanic Zone of the Andes:  
687 Insights from Boundary Element Modeling. *Tectonics*, 35(9), 1990-2013.
- 688 Suppe, J. (2014). Fluid overpressures and strength of the sedimentary upper crust. *Journal of Structural Geology*.  
689 <https://doi.org/10.1016/j.jsg.2014.07.009>.
- 690 Walter, T. R., & Amelung, F. (2007). Volcanic eruptions following  $M \geq 9$  megathrust  
691 earthquakes: Implications for the Sumatra–Andaman volcanoes. *Geology*, 35(6), 539-542.
- 692 Wendt, A., Tassara, A., Báez, J. C., Basualto, D., Lara, L. E., & García, F. (2017). Possible structural control on  
693 the 2011 eruption of Puyehue-Cordón Caulle Volcanic Complex (southern Chile) determined by InSAR, GPS  
694 and seismicity. *Geophysical Journal International*. <https://doi.org/10.1093/gji/ggw355>.
- 695 Yang X.-M., Davis P. M. (1988), Deformation from inflation of a dipping finite prolate spheroid in an elastic  
696 half-space as a model for volcanic stressing, *J. Geophys. Res.*, 93, 4249–4257
- 697 Zhan, Y., Gregg, P. M., Le Mével, H., Miller, C. A., & Cardona, C. (2019). Integrating Reservoir Dynamics,  
698 Crustal Stress, and Geophysical Observations of the Laguna del Maule Magmatic System by FEM Models and  
699 Data Assimilation. *Journal of Geophysical Research: Solid Earth*. <https://doi.org/10.1029/2019JB018681>.
- 700

701 **TABLES**

702 **Table 1.** Best fitting prolate spheroidal sources parameters. Latitude and longitude are  
 703 expressed in km (UTM WGS84 zone 18 South).

Parameter s	DSC_ STACK	95 % CI	ASC_ STACK	95 % CI	ASC ALOS1	95 % CI	DSC STACK- ASC STACK	95 % CI
Longitude (km)	736.332	(735.745;736.912)	737.680	(736.136;738.796)	737.724	(736.713;738.840)	736.598	(736.082;736.927)
Latitude (km)	5514.63	(5514.151;5515.037)	5513.53	(5512.537;5514.326)	5509.91	(5508.057;5511.366)	5514.24	(5513.952;5514.781)
Depth (km)	6	(4.530; 5.379)	1	(3.582;5.185)	5	(3.056;4.683)	4	(4.326;4.99)
Length (km)	4.965	(4.530; 5.379)	4.526	(3.582;5.185)	3.666	(3.056;4.683)	4.512	(4.326;4.99)
Dip (°)	7.600	(6.643;8.465)	9.474	(7.866;11.000)	10.395	(8.3168;12.6156)	7.768	(6.891;8.29)
Strike (°)	-2.5	(-9.2;5.7)	17.5	(10.6;20.0)	12.3	(10.2;16.3)	6.9	(-2.3;10.5)
RMS (mm)	126.9	(119.8;135.3)	126.1	(120.9;134.5)	142.3	(138.4;148.0)	129.1	(121.0;135.2)
	4.1		4.7		23.8		6.1	

704

705

706 **FIGURE CAPTIONS**

707 **Figure 1.** The Cordon Caulle volcanic complex area (PCCVC), displaying fault traces and the  
 708 last three eruptive vents. See **appendix A1** for a regional map view of structures and  
 709 seismicity in the SVZ.

710 **Figure 2.** Subset of unwrapped interferograms overlaid onto a shaded relief map. **A)**  
 711 Ascending ENVISAT encompassing the explosive eruption occurred at the beginning of June  
 712 2011, for 7-9 days. **B)** Ascending ENVISAT interferogram encompassing the effusive period  
 713 of the eruption, from June 12-13 to March 2012. The satellite to ground radar line of sight  
 714 (LOS) is shown with a black arrow. LOS displacements toward the satellite are positive (i.e.,  
 715 slant range decrease). Areas in grey correspond to low coherence areas or to areas  
 716 characterized by unwrapping errors. Coordinates are expressed in UTM-WGS84 (18 zone  
 717 South).

718 **Figure 3.** Wrapped InSAR interferograms and inversion results for a prolate-spheroidal  
 719 reservoir. Observed, modeled and residual ground displacements, for comparison between  
 720 pre- and post-eruptive periods. **Up)** ALOS1 interferograms scene pairs 07 January 2007 to 10  
 721 January 2008. **Middle)** Stack of three ascending Sentinel-1 interferograms during the post-

722 eruptive period. **Bottom**) Stack of four descending Sentinel-1 interferograms during the post-  
723 eruptive period. Each fringe (full color cycle) represents 2.83 cm (ASAR) or 11.81 cm  
724 (PALSAR) of range of change between the ground and the satellite. Areas that lack  
725 interferometric coherence are uncolored. Interferometric phase images are shown  
726 superimposed on the shaded-relief image.

727 **Figure 4.** Computed first invariant of the strain ( $I_1(\epsilon)$ ) with *Adeli*, for an overpressurized  
728 prolate-spheroidal cavity that best fits the pre-eruptive surface displacements in two  
729 configurations. **A-B**: the cavity is embedded in a homogeneous elastic medium with shear  
730 modulus  $G=20$  GPa. **C-D**: the cavity is surrounded by a weak caldera-graben domain with  
731  $G=5$  GPa embedded in a medium with  $G=20$  GPa. Areas of dilatation (positive  $I_1(\epsilon)$ ) shown  
732 in red. **A-C**) Sub-horizontal plane view following the inclined major axis of the cavity, **B-D**)  
733 Vertical cross section following profile AB parallel to the cavity's major axis.

734 **Figure 5.** Stress and strain patterns computed with *Adeli* throughout an homogeneous elastic  
735 bedrock of shear modulus  $G=20$  GPa and submitted to a (pre-eruptive) overpressure  $\Delta P$  at the  
736 walls of a prolate-spheroidal reservoir, for elastic (**A-B-C-D**) and elasto-plastic (**F-G**) media.  
737 Two vertical cross sections are displayed: AB and OP. **A-B**) First stress invariant when  $\Delta P=32$   
738 MPa : maximum  $I_1(\sigma)=13$  MPa occurs at the tips of the reservoir, where tensile failure is  
739 expected. **C-D**) The second stress invariant concentrates along the minor axis of the reservoir.  
740 **E**) Predicted modes of failure in the elasto-plastic domain depending on tensile strength ( $T$ )  
741 and cohesion ( $C$ ). The yellow circle locates the failure mode when  $T=5$  MPa and  $C=25$  MPa  
742 (friction= $0^\circ$  and no gravity), illustrated below. **F-G**) The predicted patterns of failure satisfy  
743 Eqs. (1): tensile failure represented by red regions occurs at the tips of the major axis where  
744  $I_1(\sigma) > 5$  MPa. Shear failure represented by blue regions occurs elsewhere around the  
745 reservoir where  $J_2(\sigma) > 50$  MPa. **H-I**) Shear and tensile failure patterns for an overpressurized  
746 reservoir embedded in weak caldera-graben structure with  $G=5$  GPa in contrast to the rest of  
747 the bedrock where  $G=20$  GPa, when  $\Delta P=8$  MPa.

748 **Figure 6.** InSAR best fit models for the interferogram shown Fig. 2A after removing the  
749 subsidence pattern caused by a volume change of  $\sim 0.03$  km<sup>3</sup> of the prolate spheroidal  
750 reservoir (left displays the modeled data, right displays its residual with observations). **A**)  
751 Caldera-Graben structure model. Black Line shows the geometry of the structure. Pure normal  
752 slip is imposed on the caldera border fault and reverse sinistral slip is imposed on the graben  
753 faults. **B**) Activation of a branch fault of the LOFS, along with a dextral-strike slip is imposed.

754 Black Line shows the trace of the fault. This model explains 86 % of the observed variance  
755 (rms 0.05 m). **C)** Caldera collapse and activation of the southern branch-fault only. The black  
756 rectangle represents the Okada-fault zone and the black line shows the location of the  
757 Caldera-border fault. This model explains 92 % of the observed variance (rms 0.042 m).

758 **Figure 7.** Computed first invariant of the strain ( $I_1(\varepsilon)$ ) with *Adeli*, for an overpressurized  
759 prolate-spheroidal cavity that best fits the pre-eruptive surface displacements considering a  
760 weak crustal fault zone near the cavity, with  $G=5$  GPa, and an elastic bedrock with  $G=20$   
761 GPa. **A)** Sub-horizontal plane view following the inclined major axis of the cavity. **B)** Vertical  
762 view of the fault plane along profile EF. Areas of dilatation shown in red.

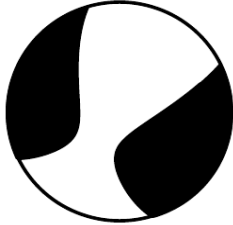

763 **Figure 8.** Patterns of stress and deformation using *Adeli* when a dextral motion of 2.5 m and  
764 75 cm is applied along the north-western and south-eastern walls of a LOFS branch-fault zone  
765 respectively, to the east of the reservoir (not overpressurized here). **A-B)** First and second  
766 stress invariants assuming an elastic bedrock, viewed along a sub-horizontal plane inclined  
767 along the reservoir's major axis. Note the reduced color palette. Maximum dilatation occurs at  
768 the fault's edges and around the reservoir nearby. Shear stress is maximum inside the fault  
769 zones and at their edges. **C)** Failure pattern assuming an elasto-plastic bedrock: plastic failure  
770 inside the two fault zones and tensile failure throughout the bedrock connecting them to the  
771 reservoir, from which dyking can be generated along two channels (1 and 2). **D-E-F)**  
772 Volumetric deformation  $I_1(\varepsilon)$  induced by the fault motion, assuming an elasto-plastic bedrock  
773 and along vertical profiles AB and OP. **D-E)** Magma potentially rises following one of the two  
774 highly dilatational channels (1 and 2). Dotted white lines indicate the fault zones intersections  
775 with profile AB. **F)** Volumetric deformation  $I_1(\varepsilon)$  at the top surface. The 2011 eruptive vent  
776 (white star) and the pre-eruptive superficial seismicity (blue points, Wendt et al., 2017) are  
777 located within the dilating area near the reservoir and the fault zone intersection.  
778

779 **Appendices**

780 **Appendix A1: 04/06/2011 Earthquake mechanism.**

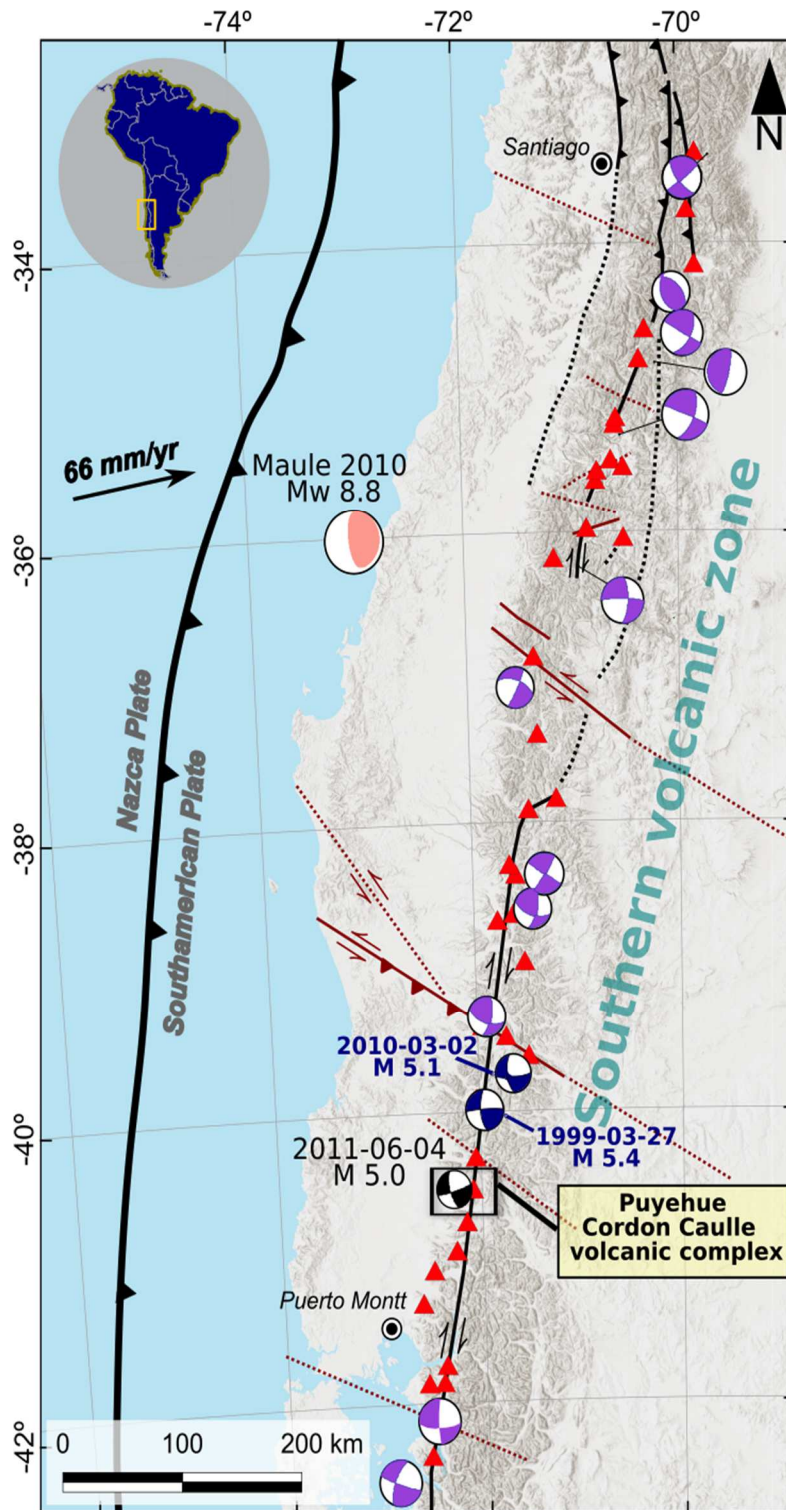
781 The GCMT project provided a solution for the largest seismic event on the day of the  
 782 eruption (at the top of table A1). In order to check the validity of the solution, we used  
 783 teleseismic data from the IRIS repository to perform a moment tensor inversion under a  
 784 probabilistic approach using the GROND software (Heimann et al, 2018). We used only  
 785 waveforms with a good signal-to-noise ratio, ensuring the best possible data fit. The best  
 786 solution is shown at the bottom of **Table A1**. It is located on the fault trace south of the  
 787 PCCVC at 7 km depth. It also shows a dextral strike-slip focal mechanism with 10% of non-  
 788 double couple component.

789 **Table A1**

Solutions	Date and time	Geometrical parameters	Focal Mechanism	Mw
GCMT solution	04-06-2011 16:28:47	Hypocentre: -40.59, -72.22 Depth : 21.2 km <b>NP1</b> : Strike : 65° Dip : 77° Rake : -27° <b>NP2</b> : Strike : 164° Dip : 74° Rake : -165°		5.0
Our solution	04-06-2011 16:28:47	Hypocentre: -40.62143, -72.11687 Depth : 7.1 km <b>NP1</b> : Strike : 250° Dip : 44° Rake : -1° <b>NP2</b> : Strike : 340° Dip : 89.5° Rake : -130°		5.0

790  
 791 Heimann, Sebastian; Isken, Marius; Kühn, Daniela; Sudhaus, Henriette; Steinberg, Andreas; Daout, Simon;  
 792 Cesca, Simone; Vasyura-Bathke, Hannes; Dahm, Torsten (2018): Grond - A probabilistic earthquake source  
 793 inversion framework. V. 1.0. GFZ Data Services. <https://doi.org/10.5880/GFZ.2.1.2018.003>





794

795 Fig. A1) Regional scale map of the Southern Volcanic zone of Chile, displaying main recent earthquakes, fault  
 796 traces and volcanic complexes. Moment tensors and their focal mechanisms were extracted from the gCMT  
 797 catalogue and includes crustal events events of  $M \geq 5$  (purple beach balls). The blue beach balls indicate crustal  
 798 events near the PCCVC, which have a similar focal mechanism to that which occurred on the day of the eruption  
 799 (indicated by a black beach ball). The 2010 Mw 8.8 Maule is indicated by the pink beach ball. Most of these  
 800 earthquakes were extracted from the collection of superficial crustal events compiled by Siefeld et al., 2019; as  
 801 well as the trace of the LOFS which is indicated by the black line with a dextral motion. ATF are indicated by the  
 802 red lines.

## 803 **Appendix A2: InSAR processing method**

804

805 All the interferograms used in this study (Table A2) were processed with the InSAR  
806 Scientific Computing Environment (ISCE) software (Rosen et al., 2012). We used the 1 arcsec  
807 Shuttle Radar Topographic Mission digital elevation model (SRTM) to remove the  
808 topographic contribution and to provide a geographic framework (UTM WGS84) for the  
809 interferograms. We used a weighted power spectral density filter (Goldstein et al., 1988) to  
810 filter the interferograms which were later unwrapped using an implementation of the  
811 Statistical cost, Network-flow Algorithm for Phase Unwrapping -SNAPHU (Chen and  
812 Zebker, 2002). The main difficulty to carry out InSAR data analysis in the study area arises  
813 from the temporal behavior of the interferometric coherence. Snow cover prevents computing  
814 interferograms during the winter months from May to November. Furthermore,  
815 interferograms from SAR images acquired during the five months of summer, show generally  
816 a reduced spatial extent of coherent area. Consequently, despite a large number of available  
817 interferograms, few interferograms are suitable for InSAR. Many coherent interferograms  
818 reveal large-wavelength phase signals or phase signals varying with topography. As the  
819 magnitude of these signals is not correlated with the perpendicular baseline, we considered  
820 that they are produced either by a change in variation of water vapor or by a pressure change.  
821 To mitigate the phase delays we corrected the interferograms using a simple empirical  
822 function that correlates phase and topography and a ramp function (linear function and a  
823 phase offset) to account for long wavelength signals after masking the area affected by  
824 displacements. This step also enabled us to estimate the uncertainty for each interferogram,  
825 and to make phase values comparable in both space and time.

826

## 827 **Table A2 InSar data**

Satellite	Orbite	Track	Start date	End date
ALOS1	Ascending	118	2007/06/23	2011/02/16
ALOS1	Ascending	119	2007/07/10	2011/03/05
ALOS2	Ascending	176	2016/07/20	2018/07/14
Sentinel-1	Ascending	164	2015/02/25	2018/12/30
Sentinel-1	Descending	83	2014/11/16	2018/09/20

828

829

830 Chen, C. W., Zebker H. A. (2002), Phase unwrapping for large SAR interferograms: Statistical segmentation and  
831 generalized networkmodels, IEEE Transactions on Geoscience and Remote Sensing, 40, 1709-1719.

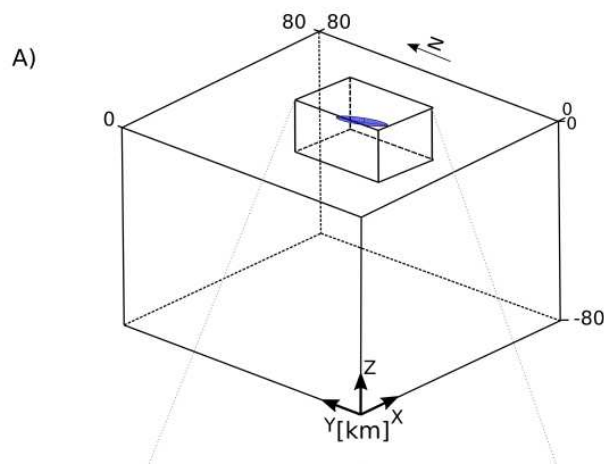
832 Rosen, P. A., Gurrola, E., Sacco, G. F., & Zebker, H. (2012). The InSAR scientific computing environment. In  
833 *EUSAR 2012; 9th European Conference on Synthetic Aperture Radar*, pp. 730-733.

834

## 835 **Appendix A3: Numerical domain setup for the three Adeli models.**

### 836 A3.1 Homogeneous Model

837 The model domain consists of a 3D block of dimensions 80×80×60 km and is meshed  
838 with the Gmsh free software (gmsh.info, Geuzaine & Remacle, 2009), with a resolution  
839 increasing from about 90 meters at the cavity walls to 8 km at the model borders. The domain  
840 borders are set free-slip except for the top free surface and the magma cavity, which remains  
841 un-meshed and whose walls are loaded with incremental overpressure ( $\Delta P$ ).



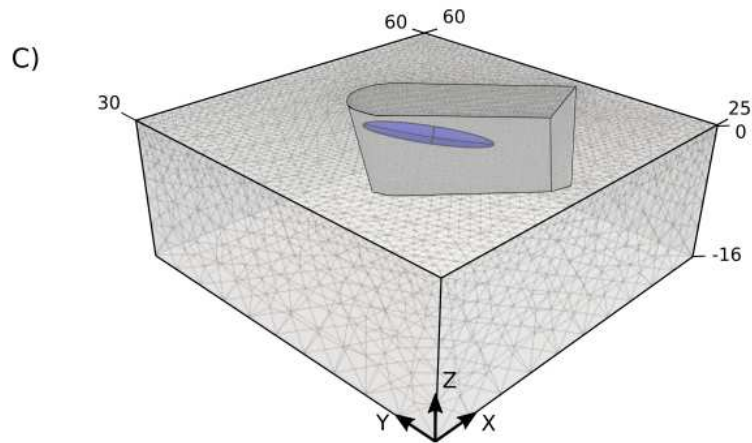
842

843 **FigA3.1** Homogeneous model. The entire mesh domain, contains only a cavity in the homogeneous  
844 case, which has the geometry of the prolate-spheroidal magma reservoir. The small parallelepiped display above  
845 only serves to separate higher and lower resolution domains.

846

### 847 A3.2 Caldera-Graben Model

848 The geometrical parameters determining the Cordillera Nevada Caldera and the  
849 northern and southern graben's walls are set based on mapped surface structures (Lara et al.,  
850 2006). Then, we extrapolate these structures at depth following the inner dipping boundaries  
851 of the caldera-graben walls suggested by Sepulveda et al. (2005) from gravity modeling. The  
852 dip angle is strongly constrained by the structure of the graben and ranges between 90 to 60 °,  
853 therefore we choose a mean value of 75°. The resulting mesh is displayed **Fig. A3.2**.



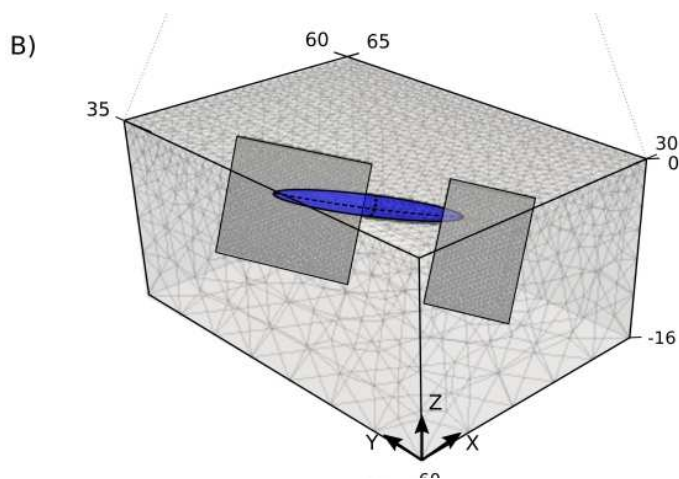
854

855 **FigA3.2** Caldera-graben mesh model.

856

857 A3.3 LOFS fault model.

858 Fault volumes are meshed with a thickness 300 m and extend over 15 km using the best fit  
 859 geometry obtained from inversions of section 6 and assuming  $G = 5$  GPa and 20 GPa in the  
 860 fault volume and bedrock, respectively. In **Fig.7** an overpressure is applied at the walls of the  
 861 cavity whereas in **Fig.8** a constant tangential velocity is applied along the western wall of the  
 862 fault zones.



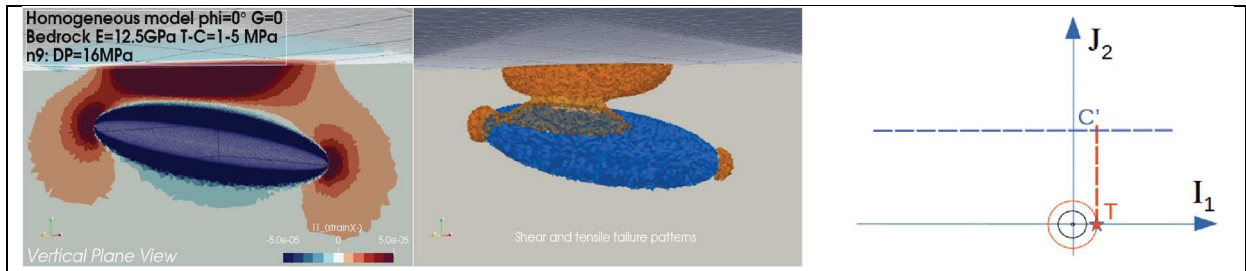
863

864 **FigA3.3** Caldera-graben mesh model.

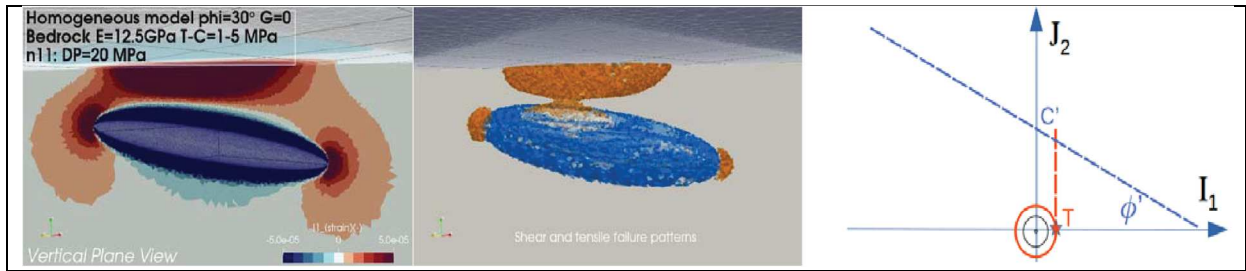
865

866 **Appendix A4:** Complementary numerical models illustrating the patterns of plastic failure  
 867 resulting from the inflation of a cavity embedded in a homogeneous crust. While the main text  
 868 assumes a Young modulus  $E=50$  GPa ( $G=20$  GPa, Fig. 6,  $T=4$  MPa and  $C=20$  MPa), cases  
 869 here have  $E=12.5$  GPa,  $T=1$  MPa and  $C=5$  MPa, variable friction angle  $\phi$ , gravity acceleration  
 870  $g$  and loading overpressure  $\Delta P$ .

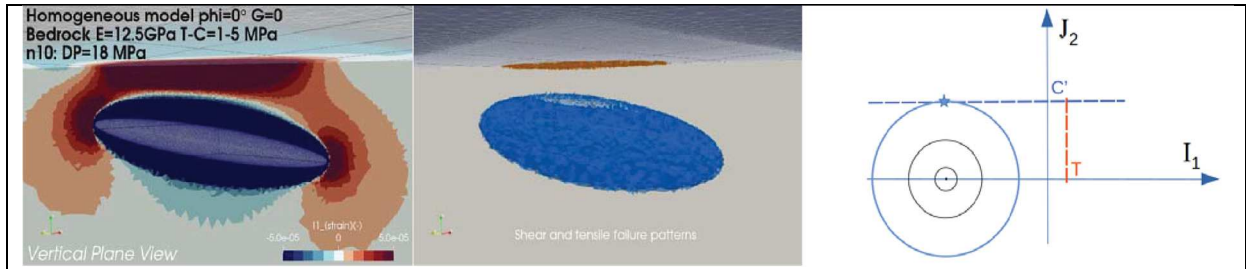
871 **a)**  $g=0$  and  $\phi=0^\circ$ , plastic connection at  $\Delta P=16$  MPa (compare with Fig. 5):



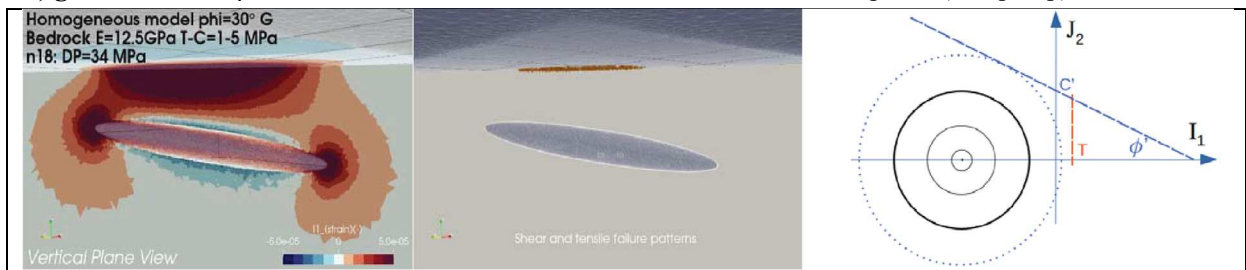
872 **b)**  $g=0$  and  $\phi=30^\circ$ , plastic connection occurs at  $\Delta P=20$  MPa, later than in a):



873 **c)**  $g=10$  m/s<sup>2</sup> and  $\phi=0^\circ$ , for  $\Delta P=18$  MPa: tensile failure is inhibited (except top), shear failure occurs.



874 **d)**  $g=10$  m/s<sup>2</sup> and  $\phi=30^\circ$ , at  $\Delta P=34$  MPa, shear and tensile failure remain impeded (except top).



875  
 876 The figures above display in vertical cross section, to the left  $I_1(\epsilon)$  (dilatation in red, color  
 877 scale ranging from  $-5.10^{-5}$  to  $+5.10^{-5}$ ), and in the center, domains of tensile (in red) and shear  
 878 failure (in blue). To the right, a schematic Mohr-circle/stress amplitude plot is drawn, with the

879 first and second stress invariants in abscissa and ordinates. This representation illustrates  
880 where failure can occur (stars) for shear and tensile failure, with tensile strength  $T$  and  
881 equivalent cohesion and friction :  $C' = \frac{6C\cos(\phi)}{3-\sin(\phi)}$ ,  $\phi' = \arctan\left(\frac{6C\sin(\phi)}{3-\sin(\phi)}\right)$ .

882 **a)** with  $g=0$  gravity and friction  $\phi=0^\circ$ , this case compares with the main text homogeneous  
883 case (**Fig. 5**) except that the bedrock here has  $G= 5$  GPa instead of  $G=20$  GPa. Hence,  
884 connection of the failure pattern between the cavity walls and the surface occurs for  $DP=16$   
885 MPa, instead of 64 MPa in the main text case. At any location point in the model the initial  
886 stress  $I_1 =0$ , and the stress circle increases (black circles) with increasing reservoir  
887 overpressure; tensile failure occurs first (red star).

888 **b)** with  $g=0$  and friction  $\phi=30^\circ$  (depth dependent condition for shear failure), the deformation  
889 and failure patterns are very similar to **a)** with tensile failure still prevailing over shear failure.

890 **c)** with  $g= 10$  kg/m<sup>3</sup> and friction  $\phi=0^\circ$ ,  $I_1$  at any depth  $z$  includes the gravity component  $\rho.g.z$ ,  
891 shifting the stress state to negative abscissas along the "Mohr-circle". Hence, the applied  
892 magma overpressure needs to overcome this constrictional stress for the stress field to reach  
893 the failure envelope. Since the shear failure threshold is low ( $\phi=0^\circ$ ), shear failure occurs  
894 around the inflating cavity while tensile failure is restricted to the surface ( $z<1$  km).

895 **d)** with  $g=10$  kg/m<sup>3</sup> and  $\phi=30^\circ$ , both shear and tensile failure thresholds require greater  
896 overpressure than in previous cases. The domain remains elastic except at the very top surface  
897 where tensile failure is still allowed.

898 The simulations in the main text assume zero-friction and zero-gravity, as in case **a)**  
899 here, and correspond to the extreme situation in which the entire crustal domain is saturated  
900 with lithostatic pore-fluid pressure (the effective mean stress vanishes, Hubbert & Rubey,  
901 1959); we are in the most favorable conditions for bedrock shear and tensile failure at lowest  
902 possible applied overpressure. Considering friction without gravity (case **b)** does not  
903 influence much the results since it only raises the shear failure yield envelope with depth.  
904 However, as soon as gravity is accounted for, the mean stress ( $I_1$ ) is shifted to negative values.  
905 Zero-friction retains the shear failure threshold to  $2C$ , but  $30^\circ$  requires the overpressure to  
906 achieve about  $1/2.\rho.g.z$  for the reservoir walls to fail (Gerbault, 2012). Hence at the shallowest  
907 reservoir tip where  $z=3$  km, the required overpressure already would have to exceed  $\sim 40$  MPa.

908  
909 Chéry, J., Zoback, M. D., & Hassani, R. (2001). An integrated mechanical model of the San Andreas fault in  
910 central and northern California. *J. Geophys. Res.* 106(B10), 22051-22066.

911 Drucker, D. C. (1951). A more fundamental approach to plastic stress-strain relations. In Proc. of 1st US  
912 National Congress of Applied Mechanics, 1951 (pp. 487-491).

913 Gerbault, M., Poliakov, A. N., & Daignieres, M. (1998). Prediction of faulting from the theories of elasticity and  
914 plasticity: what are the limits?. *Journal of Structural Geology*, 20(2-3), 301-320.

915

916 **Appendix A5: PCAIM and resolution tests for the Caldera-Graben and the LOFS**  
917 **models**

918 To solve for the slip distribution on the different fault planes used in this study, we  
919 used Principal Component Analysis-based Inversion Method (PCAIM) software package. In  
920 our models the slip distribution  $\mathbf{S}$  in elastic medium is related to the surface displacements  
921 through

$$922 \quad X_{dat} = GS \quad (A5.1)$$

923 where  $G$  is the Green function operator that gives the displacement at the measuring  
924 sites resulting from a unit slip applied on the fault and  $X_{dat}$  are the InSAR observations. To  
925 compute the Green functions, we consider point sources embedded in a homogeneous elastic  
926 half-space [Okada, 1992], assuming a Poisson coefficient of 0.25.

927 In the PCAIM algorithm, we solve for

$$928 \quad \begin{pmatrix} X_{dat} \\ 0 \end{pmatrix} = \begin{pmatrix} G \\ \gamma\Delta \end{pmatrix} S \quad (A.5.2)$$

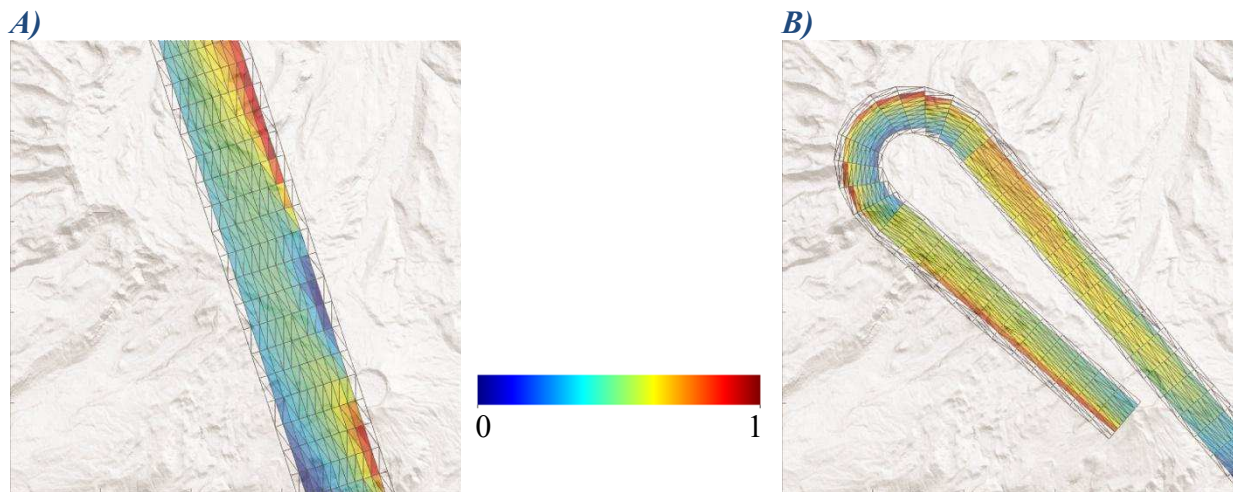
929 The Laplacian matrix  $\Delta$  is a smoothing operator regularizing the inversion and  $\gamma$  the  
930 associated parameter. The main principle of PCAIM can be found at:

931 <http://www.tectonics.caltech.edu/resources/pcaim/> and examples of applications can  
932 be found in the works of Lin et al. (2010), Perfettini et al. (2010), Remy et al. (2015).

933 Here, we detail different resolution tests that we have performed to solve for the slip  
934 distributions on the fault planes used in our study. To quantify the spatial resolution of our slip  
935 models, we compute the contribution of each patch to the total displacement of the InSAR  
936 dataset using a approach similar to that used by [Loveless and Meade, 2011; Perfettini and  
937 Avouac, 2014]. The contribution of each patch is computed considering the cumulated  
938 displacement amplitude over all observation sites due a unit of slip on this given patch. Next,  
939 the resulting field is normalized to have values between 0 and 1. The contribution of each



940 patch to the total displacement is shown in **FigA.5.1**. Patches with no color are those for  
941 which slip is not allowed.

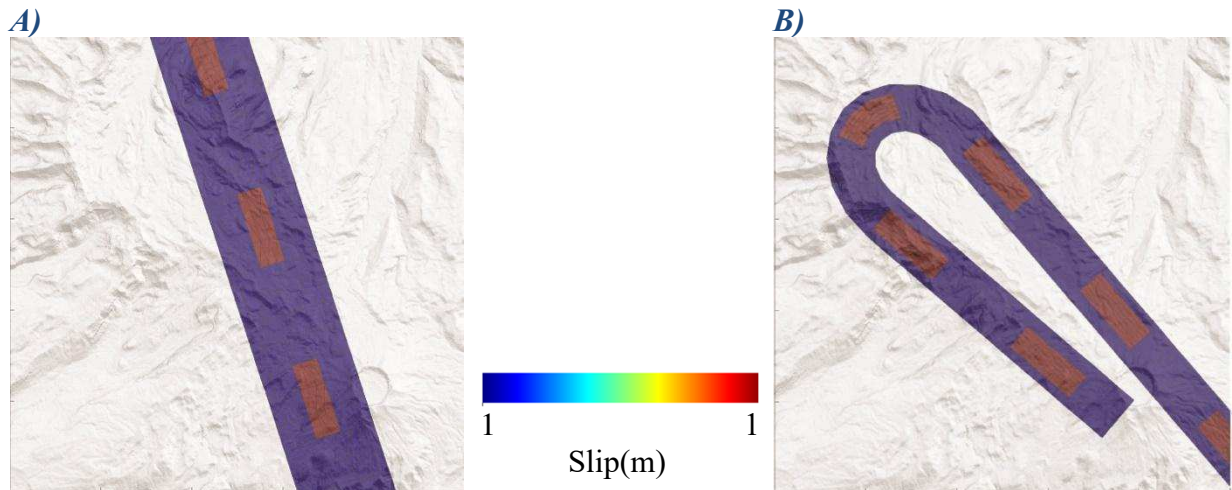


942 **Figure A5.1.** Spatial resolution of the models. A) Spatial resolution of the LOFS model. Normalized contribution  
943 of each patch to the total displacement of assuming a homogeneous slip with rake fixed to  $-165^\circ$ . B) Spatial  
944 resolution of the Caldera-Graben model assuming a normal slip for the Caldera and right lateral slip for the  
945 flank of the graben.

946 The LOFS slip model, constrained by InSAR measurements is shown in Figure 1.A As  
947 expected, the normalized contribution of the patches decreases with depth and in the region of  
948 Puyehue where no InSAR measurements are available. In the same way, the normalized  
949 contribution of the patches for the Caldera-Graben slip model decreases for the patches  
950 located in the eastern part of the study area.

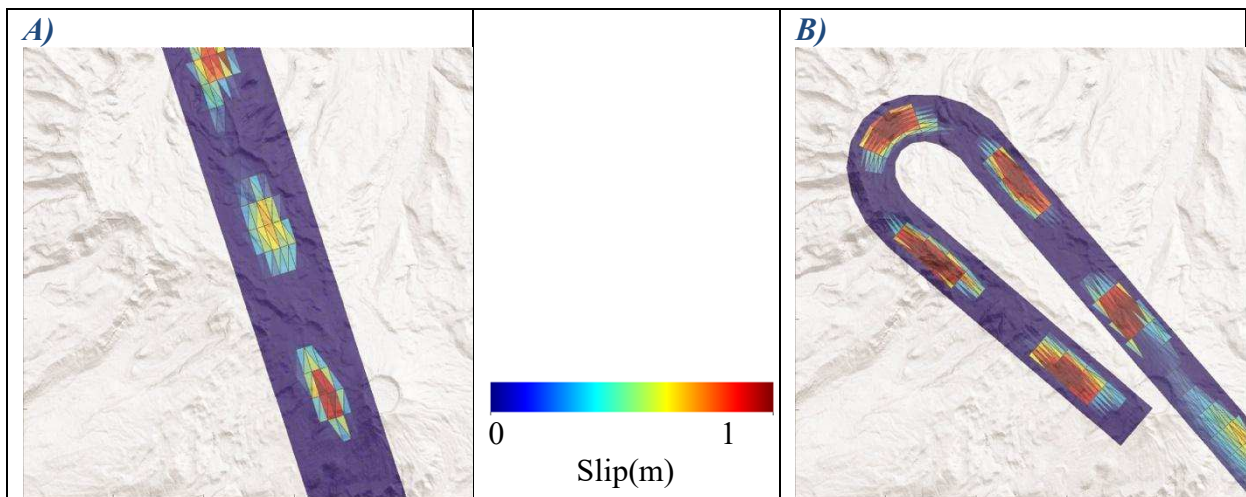
951 The spatial resolution of our model was further tested with additional resolution tests  
952 where we impose an initial slip distribution. For the LOFS model, this distribution consists of  
953 three rectangular asperities of about 4 km with unit slip. The distribution for the Caldera-  
954 Graben model consists of five rectangular asperities of about 3 km with unit slip. To the  
955 resulting modeled displacement we add a Gaussian noise with variance of  $1 \cdot 10^{-4} \text{ m}^2$ .

956 The spatial resolution of our model was further tested with additional resolution tests  
957 where we impose an initial slip distribution. For the LOFS model, this distribution consists of  
958 three rectangular asperities of about 4 km with unit slip. The distribution for the Caldera-  
959 Graben model consists of five rectangular asperities of about 3 km with unit slip. To the  
960 resulting modeled displacement we add a Gaussian noise with variance of  $1 \cdot 10^{-4} \text{ m}^2$ .

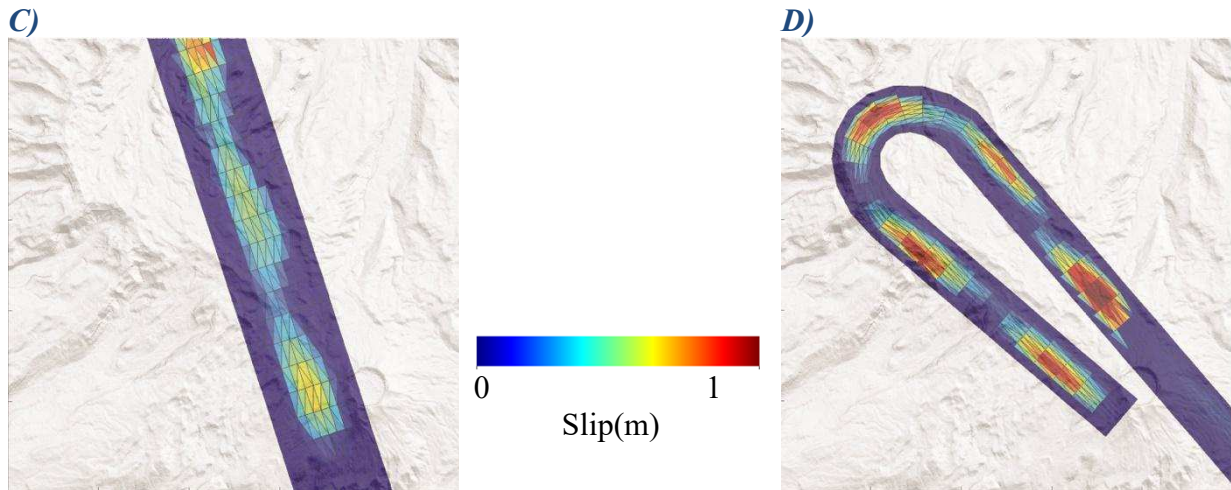


961 **Figure A5.2.** Synthetic Models. A) LOFS model. B) Caldera-Graben model.

962 The ability of our models to recover the imposed pattern, considering two values of the  
 963 smoothing parameter is shown in Fig.A5.3. Not surprisingly, rough models always allow a  
 964 better reconstruction of the initial slip distribution. The Caldera-Graben model shows a lower  
 965 ability to recover the imposed slip pattern in the eastern part of the fault plane, even using a  
 966 low value (rough model) of the smoothing parameter.



967



968

969 **Figure A5.3.** Recovered slip distributions. A and B) Using a low value of the smoothing parameter. The resulting  
 970 rms for both model is 0.01. C and D) Smooth models by increasing the smoothing parameter. The resulting rms  
 971 for these models are 0.014 and 0.015 m, respectively.

972 Lin, Yu-nung Nina, Andrew P. Kositsky, et Jean-Philippe Avouac. « PCAIM joint inversion of InSAR and  
 973 ground-based geodetic time series: Application to monitoring magmatic inflation beneath the Long Valley  
 974 Caldera ». *Geophys. Res. Lett.* 37, n° 23 (3 décembre 2010): L23301.

975 Perfettini, H., et J. P. Avouac. « The seismic cycle in the area of the 2011 Mw9.0 Tohoku-Oki earthquake ». *Journal of Geophysical Research: Solid Earth* 119, n° 5 (2014): 4469-4515.

977 Remy, D., J. L. Froger, H. Perfettini, S. Bonvalot, G. Gabalda, F. Albino, V. Cayol, D. Legrand, et M. De Saint  
 978 Blanquat. « Persistent uplift of the Lazufre volcanic complex (Central Andes): New insights from PCAIM  
 979 inversion of InSAR time series and GPS data ». *Geochemistry, Geophysics, Geosystems* 15, n° 9 (2014): 3591-  
 980 3611.